Water Practice & Technology

Water Practice & Technology Vol 18 No 8, 1898 doi: 10.2166/wpt.2023.123

Visible light treatment of azo dye-contaminated water by Ni- and Co-doped-ZnO nanoparticles supported on carbon-covered alumina

Abayomi D. Folawewo and Muhammad Dabai Bala *

School of Chemistry & Physics, University of KwaZulu-Natal, Westville Campus, Private Bag X54001, Durban 4000, South Africa
*Corresponding author. E-mail: bala@ukzn.ac.za

MDB, 0000-0002-6302-6959

ABSTRACT

Metal-ion (Co and Ni)-doped-zinc oxide (ZnO) nanocatalysts were successfully embedded onto carbon-covered alumina (CCA) supports via a simple, green sol–gel technique. The nanocatalysts were characterised by various analytical, microscopic, and spectroscopic techniques. The CCA-embedded nanocatalysts were crystalline with high surface areas and pore volume compared to the free metal-ion–doped-ZnO nanocatalysts while retaining the wurtzite phase of the core ZnO. The influences of the dopant content and the CCA on the optical and dye removal activities of the ZnO were investigated. The materials were photocatalytically active under visible light irradiation. Congo red and methyl orange dyes were used as model pollutants, and the reactivity followed a pseudo-first-order reaction kinetics. The reaction rate of the CCA-supported nanocatalysts showed doping with Co > Ni. The CCA/metal-ion-doped-ZnO was found to have photocatalytic activities better than the CCA-supported ZnO.

Key words: azo dyes, carbon-covered alumina, Ni- and Co-doping, photocatalysis, water purification, ZnO

HIGHLIGHTS

- Cost-effective ZnO is activated for visible light-responsive photocatalysis through Co/Ni + CCA incorporation.
- XRD and EDX analyses confirmed the existence of Co and Ni in ZnO sites.
- Co/Ni ion doping influenced the band gap and photoluminescence lifetime.
- ZnO–Co/CCA showed enhanced photodegradation of Congo red to 100% in 150 min and 20 times faster than with bare ZnO.

GRAPHICAL ABSTRACT

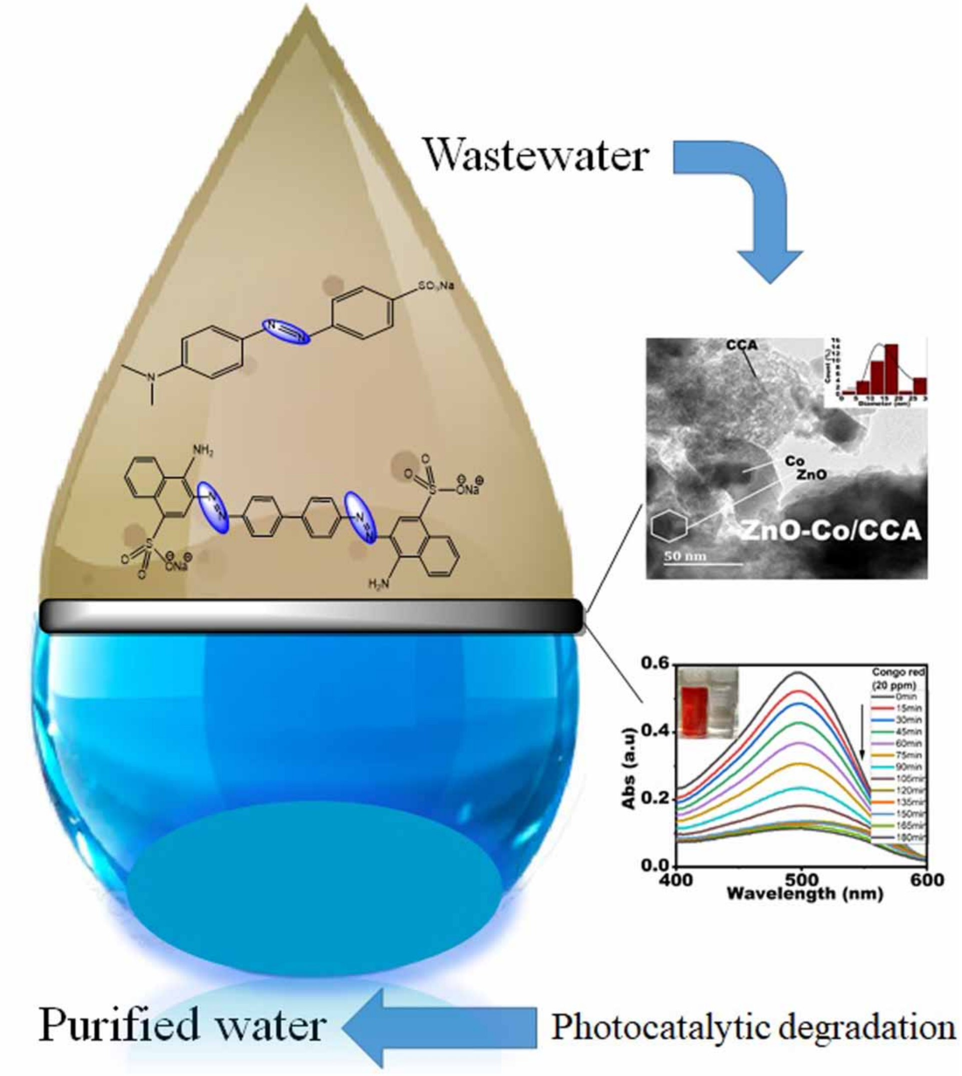

1. INTRODUCTION

Eliminating organic pollutants from wastewater is a critical step in protecting the environment. A large percentage, 15%, of all dyes produced worldwide is lost and discharged as textile waste due to the dyeing process (Pierce 1994). The removal of hazardous dyes and pigments has attracted the attention of environmental remediation efforts. Wastewaters from the dyestuff and colouring industries contain significant non-fixed chromophores, particularly azo types. Azo dyes, which contain aromatic moieties linked together by the azo (–N = N–) chromophore, are the most common dye type used in textile processing and allied industries. It has also been established that some azo dyes and their degradation products, such as aromatic amines, are highly carcinogenic (Ganesh *et al.* 1994; Zollinger 2003). Congo red (CR) is an organic compound that is the sodium salt of 3,3′-([1,1′-biphenyl]-4,4′-dial)bis(4-amino naphthalene-1-sulphonic acid), repeatedly used for a variety of industrial processes that include printing, textile colouring, pharmaceutical, and cosmetics. CR is stable, with a complex aromatic structure. It is notoriously difficult to remove mainly because it is engineered to resist fading (due to its stability to UV attack) and is also resistant to biodegradation. It is an anionic diazo dye with two azo bonds in its molecular structure, and this structural stability makes it highly toxic and resistant to degradation (Liu *et al.* 2015). Methyl orange (MO) is also an azo dye that has mutagenic properties and is hazardous on skin contact (irritant), eye contact (irritant), ingestion, and on inhalation. MO and its derivatives are carcinogenic and disrupt biological ecosystems. It can induce skin rashes, headaches, nausea, diarrhoea, muscle, and joint pain, irregular heartbeat, seizures, and toxicity to aquatic life (Yu *et al.* 2013). The discharge of these coloured wastewaters causes significant harm to aquatic life, while severe over-exposure may prove fatal if not treated timeously. The challenges of treating dyeing wastewater have resulted in sustained interest in developing advanced water purification methods. As international environmental standards have become more inflexible, more advanced technological systems for removing organic pollutants, such as dyes, have recently been developed. Many studies have been conducted to develop water dye removal techniques to meet the standards. The methods of removal are classified as:

- Physical methods: membrane filtration (Dickhout *et al.* 2017), adsorption (Değermenci *et al.* 2019), flocculation (Tang *et al.* 2016), and precipitation.
- Biodegradation: biological oxidation (Fu & Viraraghavan 2001; Senthilkumar *et al.* 2012).
- Chemical methods: photochemical decolourisation (Taka *et al.* 2017), chlorination (Miranda *et al.* 2016) and ozonation (Muñoza *et al.* 2008).

The key disadvantage of the earlier procedures is mainly that they only create a more concentrated pollutant-containing phase. Since they are not destructive but only change the contamination from one phase to another, they cause a different type of pollution and require additional treatments. Recent innovations in wastewater chemical treatment have improved the oxidative degradation of organic compounds dispersed in aqueous media. Among the new oxidation method (advanced oxidation processes-AOP), heterogeneous photocatalysis has appeared as an emerging technology leading to the most organic pollutants' total mineralisations (Fenoll *et al.* 2011; Ajmal *et al.* 2014; Anwer *et al.* 2019). Blake (1994) have provided a nearly-exhaustive list of various families of organic pollutants that photocatalysis can treat. In most cases, dissolved compounds in water are degraded using UV-illuminated titania (Blake 1994). Some recent studies (Nair *et al.* 2011; Aruna devi *et al.* 2018; Manjunatha *et al.* 2020; Reddy *et al.* 2020) have reported photosensitised degradation of organic dyes induced by visible light, which from an economic perspective, the use of solar/visible light irradiation is more encouraging than artificial UV irradiation sources.

Zinc oxide (ZnO) has been described as a viable substitute for titanium dioxide in water decontamination due to its numerous structural defects, mainly from oxygen vacancies and its ability for higher production of hydroxyl ($^{\cdot}$OH) radicals, and a photoactivity that is better by a factor of 2–3 in UV and sunlight irradiation (Udom *et al.* 2013). ZnO is a metal oxide with a large bandgap energy of 3.37 eV, a vast excitation binding energy (60 meV), n-type conductivity, abundance in nature and environmentally friendly (Dodd *et al.* 2006). Photocatalysts based on ZnO mainly absorb UV and, to some extent, visible light. It is important to note that an ideal catalyst needs to be stimulated in the visible region for practical application, especially since visible light accounts for 45% of solar radiation energy while UV accounts for only a small portion of the spectrum (Aruna devi *et al.* 2018; Sarmah *et al.* 2018). As a result, various modifications to enhance the efficiency of metal oxides are of great interest. For ZnO to be stimulated by visible light, its bandgap has to be narrowed or split into many sub-gaps, which can be accomplished by embedding transition metal ions. Doping of ZnO is an effective method to improve its catalytic activity (Manjunatha *et al.* 2020). Yarahmade & Sharifnia (2014) employed dye-sensitised ZnO nanoparticles along with phthalocyanines (Pc) co-doped with cobalt (Co) and nickel (Ni) for the photocatalytic conversion of carbon dioxide (CO_2) and methane (CH_4). Notably, the experiments were conducted under visible light conditions (Yarahmadi & Sharifnia 2014).

Similarly, Chai *et al.* (2021) employed density functional theory to examine the structural, electronic, and optical properties of an optimised ZnO monolayer doped with Co and Ni. The study demonstrates the effectiveness of strain engineering in altering the electronic characteristics of ultrathin nanofilms, thereby improving the viability of these heterojunctions for optoelectronic uses (Chai *et al.* 2021). In another study, diluted magnetic semiconductors were synthesised with 10% of Fe-, Co-, and Ni-doped-ZnO, and their semiconducting, magnetic, chemical, and optical characteristics were investigated. The results indicate that Co-doped-ZnO has the lowest band gap and average optoelectronic properties (Ghosh *et al.* 2019). Ni-doped-ZnO has been reported for the steam reforming of ethanol. There was a strong correlation between Ni loading and the selectivity of the reaction (Yang *et al.* 2006).

Besides the aforementioned, the co-doping of ZnO with Ni/Co nanomaterials to produce ZnO hybrid compounds has been reported to be effective in the photodegradation of dyes and recalcitrant organic compounds (Aruna devi *et al.* 2018; Reddy *et al.* 2020; Goktas *et al.* 2022). Cobalt and nickel have abundant electronic states and are highly compatible with the ZnO matrix for tuning its physical and chemical characteristics (Pascariu *et al.* 2018; Poornaprakash *et al.* 2020). However, adequate metal doping (optimal limit) is required to ensure that the metal particles act solely as electron traps, not recombinants, thereby aiding electron–hole separation. These metal-ion-doped-ZnO nanoparticles are visible light active and have a higher photocatalytic activity rate than bare ZnO (Aruna devi *et al.* 2018; Manjunatha *et al.* 2020; Reddy *et al.* 2020). The other method deployed to improve the photocatalytic activity of the ZnO is by combining it with other materials like activated carbon (Loo *et al.* 2018), graphite (Lonkar *et al.* 2018), carbon nanotubes (Sapkota *et al.* 2019) and alumina (Zheng *et al.* 2008). Although alumina is the most common support material, interest in carbon and carbon-covered alumina (CCA) as catalyst supports has increased in recent years. The benefits of both alumina and carbon are combined in the CCA support. Before catalyst implantation, the alumina is uniformly coated with a thin carbon layer, resulting in a support material with both the beneficial surface properties of carbon and the alumina's textural and mechanical properties (Błachnio *et al.* 2007; Zheng *et al.* 2008). The CCA has been used as a support material in hydrotreating catalysis (Maity *et al.* 2009) and ammonia preparation (Masthan *et al.* 1991). CCA supports have lately been used as packing material for HPLC (Paek *et al.* 2010) and have also been synthesised in various forms. Also, Ag nanocatalysts have been immobilised on CCA to screen microorganisms in drinking water (Shashikala *et al.* 2007). CCA-supported titania (CCA/TiO_2) (Mahlambi *et al.* 2014) nanoparticles have been used in the degradation of Rhodamine B dye under the irradiation of visible light, and metal-ion-doped-titania on CCA for the photocatalytic degradation of the same dye (Mahlambi *et al.* 2014). The incorporation of the CCA will aid in reducing electron–hole recombinations, increasing available surface area for catalysis, improved catalyst recovery and reusability, and shifting the optical response of the ZnO semiconductor to the visible light region, thus, increasing the rate of photocatalytic degradation activity (Mahlambi *et al.* 2014). The photodegradation of CR and MO dyes as major pollutant models under visible-light irradiation is used as a benchmark to test the photodegradation ability of the prepared catalysts. To our knowledge, reported herein are the first examples of effective photocatalysts based on CCA-supported ZnO-doped with earth-abundant late transition metals Co/Ni. The key aims of this report are to (i) prepare hybrid metal (Co, Ni)–doped-ZnO materials, (ii) produce the metal-doped-ZnO–CCA heterostructured composite in which the metal-doped-ZnO is embedded in the CCA, (iii) improve nanocatalyst recovery and reusability in the photodegradation of CR and MO dyes, and (iv) further expand the optical absorbance of the metal-doped-ZnO/CCA nanocatalyst into the visible light region, thereby improving photocatalytic performance.

2. MATERIALS AND METHODS

2.1. Materials

All reagents were of analytical grade. Zinc acetate, cobalt acetate, nickel acetate, calcium hydride, potassium chloride (99%), and oxalic acid were purchased from Industrial Analytical (South Africa). Capital Research Distributor Co., Ltd (South Africa) supplied absolute ethanol (EtOH), CR, and MO dyes. Sulphuric acid (98%), γ-alumina (calcined at 500 °C for 3 h to remove any organic impurities), disodium ethylene tetraacetic acid (EDTA), *n*-xylene (dried on calcium hydride overnight before usage), *p*-benzoquinone (BQ), and toluene 2,4-diisocyanate (TDI, used without purification) were purchased from Merck (Pty) Ltd. Analytical grade n-propanol and isopropyl alcohol (IPA) were purchased from Industrial Analytical (Pty) Ltd. IPA was distilled before usage.

2.2. Preparation of ZnO and metal-Ion–doped-ZnO

ZnO was synthesised by the sol–gel method. A solution (tagged A) was prepared from 0.01 mol of zinc acetate dissolved in 60 mL of EtOH and stirred at 60 °C for 30 min. Then another solution (tagged B) was made by dissolving 0.02 mol of oxalic acid dihydrate in 80 mL of EtOH and stirring at 50 °C for 30 min. Solution B was added to the warm solution A dropwise and stirred for 1 h. A white sol was obtained, aged, and dried at 80 °C for 24 h. Finally, ZnO was obtained by calcination at 450 °C (Chen *et al.* 2017).

The metal-ion-doped-ZnO was prepared by modifying the method reported by Chen *et al.* (2017): A solution (A) was made from 0.01 mol of zinc acetate dissolved in 60 mL of EtOH. Then, 0.02 mol of cobalt acetate or nickel acetate (at various mole percentages) was dissolved in EtOH and added in drops to solution A, stirred at 60 °C for 30 min. A second solution (B) was obtained by dissolving 0.02 mol of oxalic acid dihydrate in 80 mL of EtOH, stirred at 50 °C for 30 min, then dropwise added to warm A and stirred for 1 h. A coloured sol was obtained, aged and dried at 80 °C for 24 h. The metal-doped-ZnO was obtained by calcination at 450 °C (Chen *et al.* 2017).

2.3. Synthesis of CCA supports

CCA supports were prepared by modifying the adsorption–pyrolysis method. A blend of γ-alumina (5 g) and 1% TDI in *n*-xylene (115 mL) were stirred at ambient temperature for 24 h. The resulting mixture was filtered and washed severally with *n*-xylene (100 mL). A feathery white precipitate was obtained and dried overnight at 80 °C. The precipitate obtained was then pulverised and placed into a quartz cell. The temperature was gradually increased to 700 °C under a nitrogen flow (30 mL/min^{-1}) and held at the same temperature for 3 h to complete the pyrolysis of TDI (Sharanda *et al.* 2006).

2.4. Preparation of CCA-metal-doped-ZnO (ZnO-M/CCA)

A colloidal suspension of the metal-ion-doped-ZnO (ZnO-M) in deionised water was prepared and sonicated for 30 min at ambient temperature, followed by the addition of the CCA, sonicated for 1 h and left at ambient temperature for 24 h to dry. The resulting product was dried at 80 °C overnight to yield the ZnO-M/CCA, which was then pulverised and treated at 450 °C for 3 h to afford the metal-doped-ZnO-impregnated CCA support (Sharanda *et al.* 2006).

2.5. Chemical oxygen demand analysis

Chemical oxygen demand (COD) analysis was determined using COD vials purchased from Merc, Inc. South Africa (COD Cell Test 10–150 mg/L with product number: 1.14540.001). COD is generally used to determine the content of oxidisable organic matter in a wastewater sample. For this, 3 mL of the sample wastewater was dispersed into the COD vials and vortexed for 2–3 min to ensure thorough sample mixing with the COD reagents. The sample was then digested in a thermoreactor at 148 °C for 2 h and allowed to cool down before determining the value of the COD using the control cuvette to zero the instrument (Spectroquant NOVA 60). The test results were expressed as mg/L COD, and COD per cent reduction was calculated using Equation (1) (Morshed *et al.* 2019):

$$\mathrm{COD}(\%) = \frac{\mathrm{COD}_0 - \mathrm{COD}_t}{\mathrm{COD}_0} \times 100 \tag{1}$$

where COD_o and COD_t are the initial COD and COD at time *t*, respectively.

3. MATERIAL CHARACTERISATION

Homogeneous powders of various samples were loaded into the sample holder on a glass slide and levelled to the correct height of a multi-purpose X-ray diffractometer D8-Advance (manufactured by Bruker AXS-, Germany) operated in a continuous ϑ-ϑ scan in locked coupled mode with Cu-K_α radiation. The measurements run within a range in 2ϑ defined by the user with a typical step size of 0.034° in 2ϑ ($\lambda K\alpha_1 = 1.5406$ Å). A position-sensitive detector, Lyn-Eye, is used to record diffraction data at a regular speed of 0.5 s/step, equivalent to an adequate 92 s/step time for a scintillation counter. A Spectrum 100 spectrophotometer (Perkin Elmer, USA) acquired the FTIR spectra at room temperature using an attenuated total reflectance (ATR) sampling accessory. All spectra were acquired in transmission mode in the 400–4,000 cm^{-1} range, with 32 scans and a resolution of 2.0 cm. To determine the surface area (S_{BET}), pore volume, and pore size distributions of the as-prepared samples, a Micromeritics TriStar II (USA) surface area and porosity analyser was used. The sample was degassed in N_2 under vacuum for 24 h at 200 °C before the analysis. Typically, the sample was heated to 90 °C at a heating rate of 5 °C min^{-1} and held at the same temperature for 180 min. The sample was then evacuated at a pressure of 50 mmHg for 30 min. The temperature was then ramped to 180 °C at a heating rate of 10 min^{-1} and degassed for 24 h under N_2. The microstructure and morphology of the nanocatalysts were studied utilising Carl Zeiss Ultra Plus FEG (Germany) fitted with an energy-dispersive Oxford X-max detector (United Kingdom).

Similarly, for scanning electron microscopy (SEM), with an operating voltage of 30 kV, and transmission electron microscopy (TEM) operating at both standard and high-resolution (HR-TEM) modes with an operating voltage of 200 kV, a JEOL JEM 2100 (JEOL Ltd, Japan) was used. Before the TEM analysis, the powdered samples were dispersed in EtOH and sonicated for 15 min, after which the sample holder (grid) was dipped into the dispersion. The sample holder was removed and dried with a UV lamp before reinsertion into the TEM sample port for imaging. The SEM and TEM equipment were outfitted with an EDX detector, which was used to identify all the prepared samples. The photoluminescence (PL) spectra were collected using a

Perkin Elmer LS 55 (USA) spectrofluorimeter with an excitation wavelength of 325 nm and emission slit widths of 10 nm. The PL spectra were acquired in the wavelength range 390–800 nm, and a few mg of the sample powder was placed in a sample holder for the PL studies. UV/Vis reflectance spectra were collected using a Perkin Elmer Lambda 55 (USA) UV–Vis spectrophotometer equipped with an integrating sphere (Labsphere-USA). Bandgap energies were calculated by plotting $(F(R)\text{-}h\upsilon)^2$ against hυ from the corresponding Kubelka–Munk functions (F(R), which are directly proportional to radiation absorption. The electrochemical measurements were carried out with a VersaSTAT 3F electrochemistry workstation (AMETEK Scientific Instruments, USA). A three-electrode system consisting of a reference, counter and working electrodes was employed. The working electrodes were made by modifying glassy carbon electrodes (GCE) with the respective photocatalysts (ZnO and ZnO-M/CCA). The modification typically involved adding ethanol (600 μL) to a mixture containing a 10 mg sample and 3 mg carbon paste (binder) and sonicated for 30 min. The resulting mixture was drop-casted with a micropipette onto a clean, glassy carbon electrode and allowed to dry overnight. A platinum wire was used as the counter electrode, and Ag/AgCl was the reference electrode. A 0.5 M of Na_2SO_4 solution was used as the electrolyte. Any dissolved oxygen in the solution that would otherwise interfere with the redox activity of the working electrode during measurements was purged out by pumping nitrogen gas through the system for 5 min. The electrochemical impedance spectroscopy (EIS) measurements were performed using the same three-electrode system (Yang *et al.* 2021). The thermal stability of the samples was determined with a thermogravimetric analyser with a small furnace (SF) (Mettler Toledo-Germany). The TGA was measured at a heating rate of 10 °C/min from 25 to 800 °C in air.

3.1. Photocatalytic degradation studies

3.1.1. Photocatalytic set-up

A commercial fluorescent lamp (3 U E27 32w, cool white, 8,000 h) with an optical filter to cut-off UV light was used in a closed photocatalytic chamber for the photocatalytic reactions. The light intensity at the reaction position is 880 W/m^2 without a filter and 830 W/m^2 with the UV cut-off filter ($\lambda > 420$ nm). An Oriel 70260 Radiant Power meter measured the intensities, with a 10 cm distance between the light source and the reactor. The photocatalytic properties of the materials were determined on 100 mL (20 mg L^{-1}) dyes. The prepared ZnO-M/CCA materials (10 mg per 100 mL of 20 mg L^{-1} dye) were used in the suspension. The set-up was agitated over a magnetic stirrer for 30 min before exposure to the lamp to balance adsorption–desorption between the dye and the photocatalyst. Aliquots of 4 mL were collected from the reactor at 15-min intervals to determine the amount of dye removed. The sample was centrifuged at 6,000 rpm for 15 min before absorbance measurements, and the supernatant was filtered via a 0.45-μm microfilter to remove the catalyst. The absorbance of the filtrate was measured at λ_{max} of 498 nm for CR and 465 nm for MO. Equation (2) was used to compute the percentage removal of dyes over time. The set-up was the same for both the ZnO-M and ZnO-M/CCA (1:2) materials:

$$\left(\frac{C_o - C_t}{C_o}\right) \times 100 \tag{2}$$

C_o is the dye's initial concentration (mg/L) before exposure to visible light and C_t is the concentration at time t. For the recyclability test, the best catalyst was recovered, and the procedure described was repeated under the same settings for four more catalytic runs to study its stability. All catalytic data are run in duplicates.

4. RESULTS AND DISCUSSION

4.1. Structural properties

4.1.1. XRD analysis

The powder X-ray diffraction (PXRD) diffractograms [Figure 1(a) and 1(b)] display the XRD analysis results for the prepared samples [ZnO–Co (0.5:0.1)/CCA (0.1:1) and ZnO–Ni(0.5/0.25)/CCA(0.75:1)-most active]. The PXRD diffractogram of the CCA support does not show peaks linked with ordered carbon structure, indicating that it is most likely in the amorphous form or a thin graphitic layer in the CCA (Sharanda *et al.* 2006; Liu 2011). XRD can only detect graphite loads with a thickness of at least 3 nm, corresponding to approximately 10 layered graphene sheets. For the CCA sample, highly defective and nanosized carbon particles were present (Mendes *et al.* 2020; Sun *et al.* 2020; Kazakova *et al.* 2021). The only peaks that could be seen are those associated

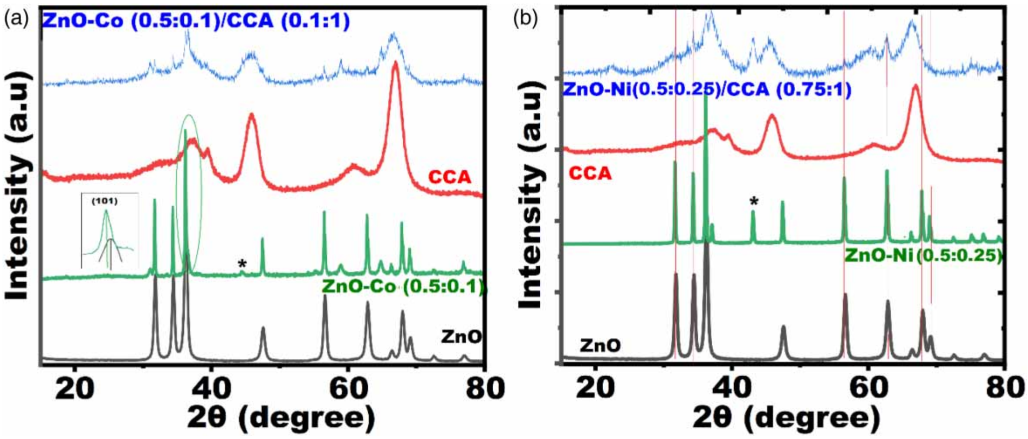

Figure 1 | PXRD of (a) ZnO–Co and (b) ZnO–Ni, each with the diffractograms of ZnO and CCA for comparison (shift to lower diffraction angles shown as an inset in (a)). Please refer to the online version of this paper to see this figure in colour: https://dx.doi.org/10.2166/wpt.2023.123.

with the alumina at $2\theta = 32.61$ (220), 37.28 (311), 39.50 (222), 45.93 (400), 60.66 (333), and 66.92 (440), which corresponds to the PXRD data obtained from the JCPDS card no. 00-047-1308.

The diffractogram of ZnO displays characteristic sharp and well-defined peaks at $2\theta = 31.77$, 34.38, 36.29, 47.59, 56.63, 62.88, 66.37, 67.99, and 69.15, marked by their miller indices [(100), (002), (101), (102), (110), (103), (200), (112) and (201)] referred to the existence of ZnO nanoparticles with hexagonal wurtzite structure (JCPDS no. 00-036-1451) with ($a = b = 3.24982$ Å, and $c = 5.20661$ Å) with a preferential orientation of (101) plane with respect to other planes. No other impurity peaks were detected, indicating that the obtained ZnO was phase pure. While the data for both the ZnO–Co/CCA and ZnO–Ni/CCA composites show peaks associated with metal-doped-ZnO as observed (ZnO traced with the red line, blue line for CCA and aqua line for Ni ions). Additionally, the Ni^{+2} (200) phase peaks around 44° and Co^{+2} at 43° were detected on the diffraction patterns of ZnO–Co/CCA and ZnO–Ni/CCA composites, respectively (designated '*').

The most intense peaks of both ZnO and metal-doped-ZnO corresponding to (100), (002) and (101) phases were broadened and found to reduce in intensity due to the transition metal dopants in ZnO–Co/CCA and ZnO–Ni/CCA. A progressive shift to lower diffraction angles of the peak indexed to the (002) phase is also observed (as the inset in Figure 1(a)) (Estévez-Hernández *et al.* 2017). The shifting of peak position is ascribed to induced internal strain in the lattice due to the substitution by smaller Co/Ni ions in the ZnO framework [ionic radius difference between Zn^{+2} (0.74 Å) and Co^{+2} (0.65 Å), Ni^{+2} (0.55 Å) ions] (Kalita & Kalita 2017).

The average crystallite size for the ZnO, ZnO–Co/CCA and ZnO–Ni/CCA composite were calculated using the Debye–Scherrer equation formula (Equation (3)):

$$D = \frac{k\lambda}{\beta\cos\theta} \tag{3}$$

where D is the average crystal size of the catalyst, λ (nm) is the wavelength of the X-ray, β is the width of the XRD peak at full width at half maxima (FWHM), and k is the factor which is approximated as 0.9, and θ is the diffraction angle. The prepared samples' calculated average crystallite size are 15.52, 15.27, and 16.77 nm for ZnO, ZnO–Co/CCA, and ZnO–Ni/CCA, respectively. Furthermore, the crystallinity index for the ZnO, ZnO–Co/CCA, and ZnO–Ni/CCA were determined as 85, 80, and 76%, respectively, suggesting that the embedding of the semiconductor onto CCA did not impact the crystal nature of the material. The average crystallite size of ZnO was in close agreement with published data (Ong *et al.* 2018). Furthermore, the interlayer spacing was calculated by (Equation (4)):

$$d = \frac{n\lambda}{2sin\theta} \tag{4}$$

where d is the interlayer spacing, n ($n = 1$) is the order of diffraction, λ (nm) is the wavelength of incident X-ray, and θ is the diffraction angle in radians. The average d-spacing for ZnO–Co/CCA and ZnO–Ni/CCA was estimated as 0.180 and 0.255 nm, respectively.

4.1.2. Surface area and porosity

The surface area (BET) and porosity were calculated using nitrogen (N_2) adsorption–desorption isotherms at 77 K. The BET isotherms of all prepared samples (Alumina, CCA, ZnO–Co (0.5:0.1)/CCA (0.1:1) and ZnO–Ni (0.5:0.25)/CCA (0.75:1) are shown in Figure 2 and Supplementary material, Figure S1, with the pore size distribution plots as insets, with the key data summarised in Table 2.

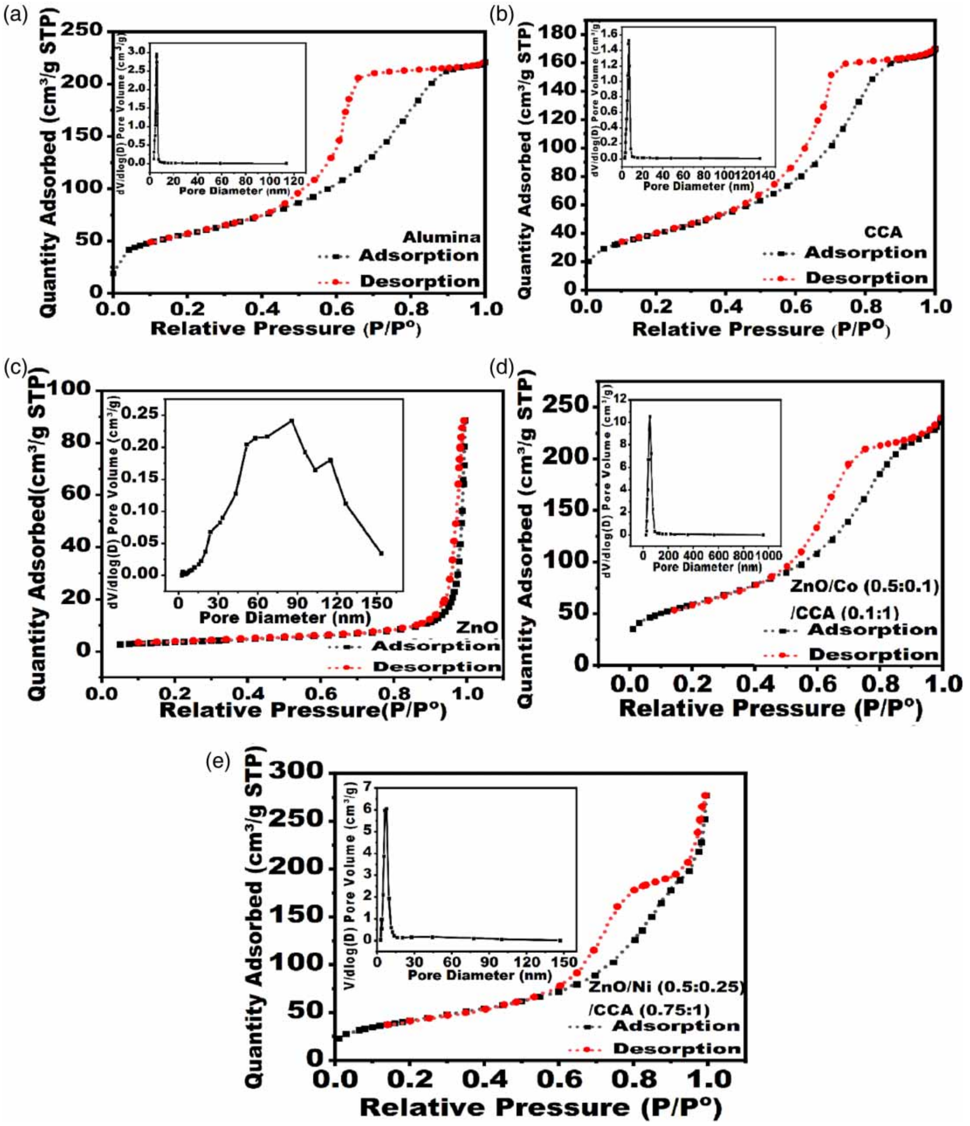

Figure 2 | BET isotherms and the Barrett–Joyner–Halenda (BJH) pore volumes [as inset] of (a) alumina, (b) CCA, (c) ZnO, (d) ZnO–Co (0.5:0.1)/CCA (0.1:1), and (e) ZnO–Ni (0.5:0.25)/CCA (0.75:1) mass fraction.

The surface area, pore volume, and pore size distribution were chosen to study the effect of carbon loading on the alumina surface, metal-doped-ZnO, and the effect of embedding the metal-doped-ZnO nanomaterials on the CCA (Table 1). The adsorption–desorption isotherms of alumina, CCA, ZnO, ZnO–Co (0.5:0.1)/CCA (0.1:1), and ZnO–Ni (0.5:0.25)/CCA (0.75:1) are depicted in Figure 2(a)–2(e). The alumina, CCA, ZnO–Co/CCA, and ZnO–Ni/CCA composite all have heterogeneous pore structures and adsorption–desorption isotherms classified as type IV according to the Brunauer–Emmett–Teller (BET) classification, indicating that they are mesoporous

Table 1 | Structural and textural properties of the ZnO, ZnO–Co/CCA, and ZnO–Ni/CCA samples

Entry	Sample	Crystallite size (nm)	S_{BET} (m^2g^{-1})	Total pore volume (cm^3/g)	Pore size (nm)
1	Alumina	2.63	202.55	0.387	6.27
2	CCA	2.55	144.62	0.297	6.50
3	ZnO	15.52	13.78	0.259	4.30
4	ZnO–Co/CCA	15.27	213.93	10.54	54.33
5	ZnO–Ni/CCA	16.77	152.37	6.05	7.50

Table 2 | Photocatalytic activity of the metal-doped-ZnO/CCA compared with TiO_2-based systems

Photocatalyst	Light source	Method of synthesis	Pollutant (mgL^{-1})	Degradation (%)	Degradation time (min)	Ref
TiO_2/CCA (100 mg)	Solar	Precipitation/ Calcination	RhB	100	270	Mahlambi *et al.* (2014)
TiO_2-M/CCA (100 mg)	Vis	Precipitation/ Calcination	RhB (10 mgL^{-1})	100	180	Mahlambi *et al.* (2013)
ZnO-M/CCA (10 mg)	Vis	Sol–gel/Calcination	MO and CR (20 mgL^{-1})	100 and 98	180	This work

RhB, Rhodamine B; MO, methyl orange; CR, Congo red; M, Co, Ni.

materials. Adsorbent–adsorptive interactions and interactions between molecules in the condensed state determine the adsorptive nature of mesopores. Mesoporous materials have properties that include pore condensation, a process in which a gas condenses into a liquid-like phase in a pore at a pressure P less than the saturation pressure P_0 of the bulk liquid (Monson 2012; Landers *et al.* 2013). ZnO revealed bimodal pore size distribution and a type H3 hysteresis loop linked with capillary condensation and multilayer adsorption on the nanocatalyst surface.

The mesoporous structure of ZnO allows pollutants to disperse through its channels and be destroyed on the catalyst surface. All prepared samples feature a large hysteresis loop, with alumina having $P/P_0 = 0.4–0.9$, indicating that it is mesoporous and has a high adsorption capacity (219 cc/g at $P/P_0 = 1$). In contrast, the CCA exhibited (170 cc/g at $P/P_0 = 1$) with similar hysteresis loop. Following impregnation, the formed ZnO–Co/CCA (240 cc/g at $P/P_0 = 1$) and ZnO–Ni/CCA (270 cc/g at $P/P_0 = 1$) also have large type H2 hysteresis loops of $P/P_0 = 0.5–0.9$ with the highest adsorption capacity. This type of isotherm describes the process of nitrogen adsorption on the material's surface. In addition, this type is linked with a sharp desorption branch at relative pressures near the lower end of hysteresis (adsorption–desorption). The highly steep desorption observed in H2 loops can be ascribed to pore-blocking/percolation in a narrow range of pore necks or cavitation-induced evaporation. Furthermore, when compared to pure ZnO, the ZnO–Co/CCA and Zn–Ni/CCA catalysts had higher specific surface area and pore volumes. In comparison, CCA has a surface area of 144.62 m^2g^{-1}, similarly observed previously (Souza Macedo *et al.* 2019; Mendes *et al.* 2020; Kazakova *et al.* 2021). ZnO had an active area value of 13.78 m^2/g^{-1}. In contrast, ZnO–Co/CCA and ZnO–Ni/CCA have surface areas of 213.93 and 152.37 m^2/g^{-1}, respectively, which are wider and better for more active reaction sites and the separation of photogenerated excitons. The observed increase in the active area for ZnO-M/CCA compared to bare ZnO is due to the carbon loading, consistent with previous research (Mahlambi *et al.* 2014; Lin *et al.* 2019). As a result, the available active area for dye adsorption and removal increases. According to the BET grouping (Sing *et al.* 1985), it has channel-like pores with non-uniform pore size distribution within the mesoporous regions (Nishikiori *et al.* 2012; Thommes *et al.* 2015).

4.2. Morphological surface studies

4.2.1. SEM, TEM, and EDX spectroscopy

SEM, and transmission electron microscope (TEM), were used to study the surface morphology of the various materials reported herein. In addition, the high-resolution transmission electron microscope (HR-TEM) and the energy-dispersive X-ray analysis (EDX) were used to study the microstructure and surface chemistry. The images in Figure 3 display the SEM results, Figure 4 displays the TEM images, and Figures 4 and 5 display the HR-TEM analysis data for all the synthesised materials. The EDX is presented in Supplementary material, Figure S5.

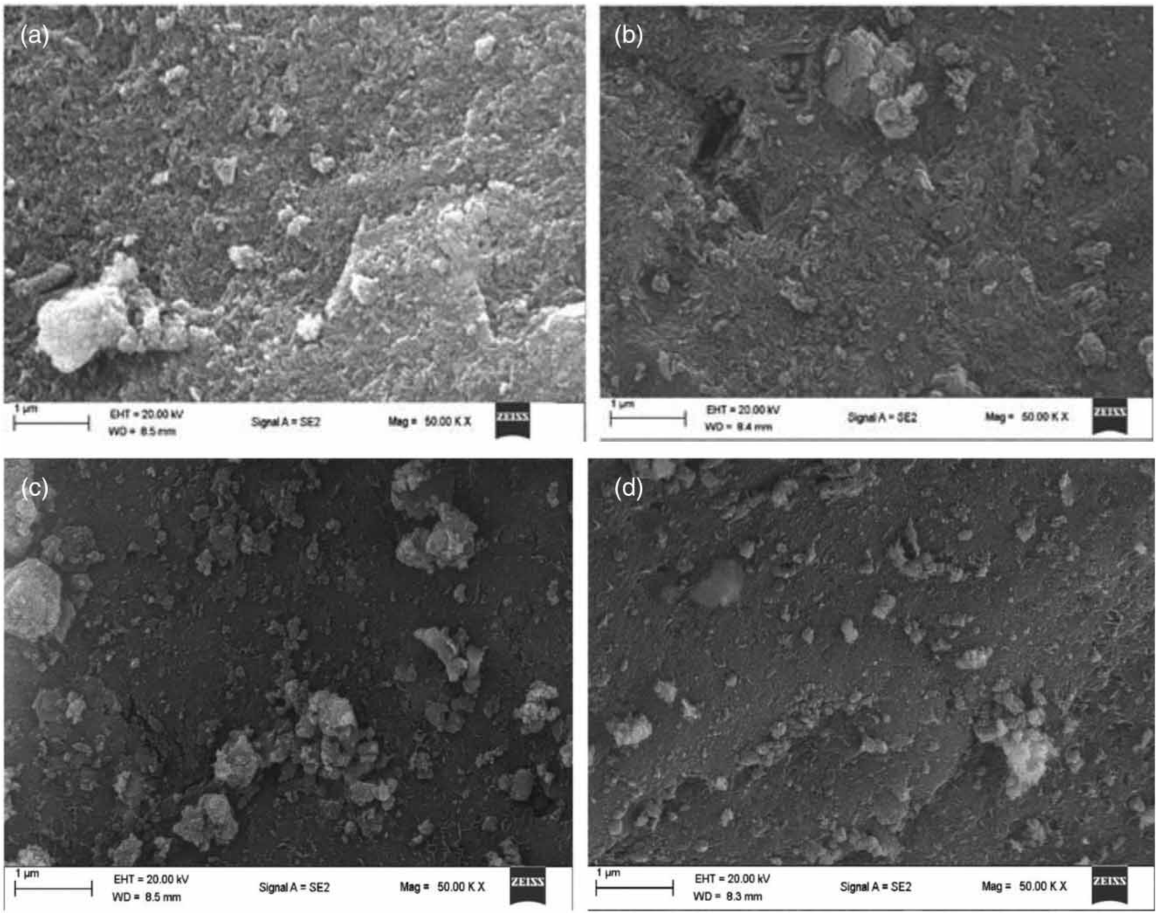

Figure 3 | SEM micrograph for (a) alumina; (b) CCA; (c) ZnO–Co/CCA; and (d) ZnO–Ni/CCA.

The SEM image of alumina (Figure 3(a)) shows that it is made up of large particles on a granular surface with a size distribution between 21 and 23 nm. In contrast, the CCA surface seen in Figure 3(b) is smooth and porous due to the homogeneous covering of carbon. The ZnO's SEM image showed spherical and clustered particles due to calcination (Behnajady *et al.* 2011; Bekele *et al.* 2021). Figures 3(c) and 3(d) represent the hybrid combination of the Ni and Co ion-doped-ZnO catalyst on the CCA surface. The images of the Co and Ni-doped-ZnO catalysts supported by CCA are similar and show uniform dispersion of the metals in the matrices of the ZnO–Ni/CCA and ZnO–Co/CCA heterostructures.

TEM was used to further investigate the differences in crystal arrangement. The micrograph of the ZnO revealed the typical crystalline hexagonal wurtzite structure (at a higher magnification of 50 nm (Figure 4(a)). The 'hexagonal' structure of ZnO is clearly seen (indicated by white hexagonal shape). The ZnO–Co (0.5:0.1)/CCA (0.1:1) and ZnO–Ni (0.5:0.25)/CCA (0.75:1) were selected for the TEM and HR-TEM study. Figures 4(c) and 4(d) show well-separated grains with hexagonal and spherical structures on the surface. Also, Figure 4(b) displays the TEM image of the CCA support, which shows that it is microporous and fluffy due to the carbon covering. The triangular sublattice of complete graphene is well understood to comprise equivalent carbon atoms. However, the sublattice composition of defective graphene may differ, resulting in corresponding changes in the carbon content of a monolayer coating of disordered carbon material, as seen in the TEM image (Figure 4(b)), confirming the XRD analysis (see Supplementary material, Figure S4(b)) (Kazakova *et al.* 2021).

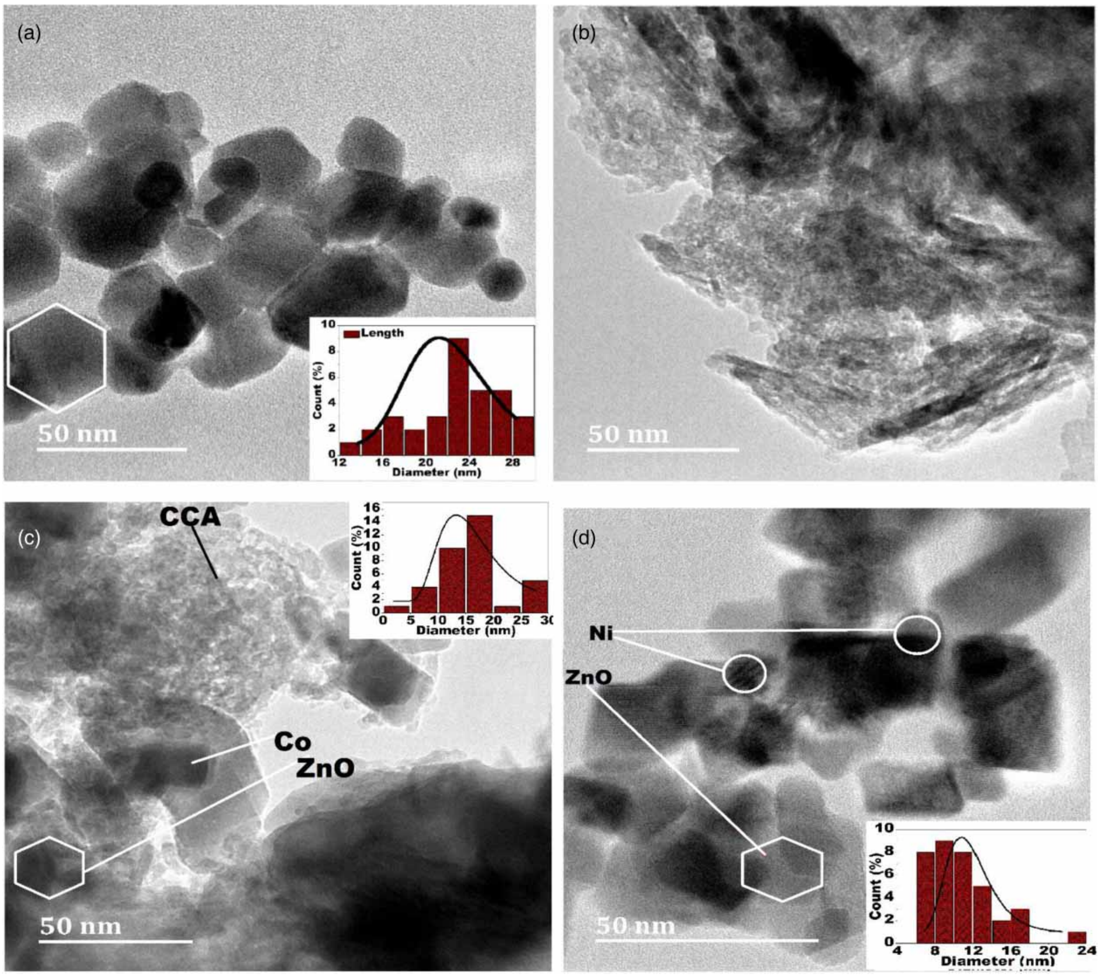

Figure 4 | TEM image of (a) ZnO; (b) CCA; (c) ZnO–Ni/CCA; and (d) ZnO–Co/CCA.

Since metal ions are incorporated into the ZnO lattice, and the CCA supports are made of an amorphous carbon layer, it is critical to maintaining the crystallinity of the nanoparticles because it is directly responsible for their catalytic activity. The metal-doped-ZnO were uniformly distributed on the CCA supports, a common unique feature of the CCA supports (Lin *et al.* 2005; Shashikala *et al.* 2007). This observation may be due to the porosity of CCA, which enabled the even distribution of the embedded catalysts. In addition, the CCA-supported catalyst did not lose crystallinity, which agrees with the PXRD data. The average interlayer spacing was determined as 0.214 nm for ZnO–Co/CCA and 0.199 nm ZnO–Ni/CCA, which agrees well with the 0.255 and 0.180 nm obtained from the XRD data, respectively. In addition, the particle size of ZnO–Co/CCA and ZnO–Ni/CCA range from 10–12 and 10–15 nm, respectively, in close agreement with the PXRD data. The metal-ion-doped-ZnO catalyst appears to be set in the pores of the CCA, signifying that they can be used in catalysis without unravelling from the support.

Additionally, the HR-TEM images of ZnO–Co/CCA and ZnO–Ni/CCA in Figures 5(a) and 5(b) reveal concentric rings indicating polycrystallinity (a blend of amorphous and crystallinity) in the nanocomposite. It comprises many crystallites, and discrete spots that make up the rings. Furthermore, the observed selected area electron diffraction (SAED) pattern differs from pure hexagonal ZnO (Supplementary material Figure S4), indicating the formation of metal-doped-ZnO nanocomposites. Similarly, Figures 5(c) and 5(d) show the determined d-spacing.

Supplementary material (Figure S5) shows the EDX spectra of the two-metal-(Co and Ni)-doped-ZnO supported on the CCA, confirming that the as-prepared sample contains only Zn, O, Ni, Al, C, and Co ions in the samples. In addition, the elemental mapping images in Supplementary material, Figures S5(d)–5(h) show that Al, O, Zn, and C elements are spatially and homogeneously distributed in the maps. These results agree with the PXRD data; no other impurity phases were found.

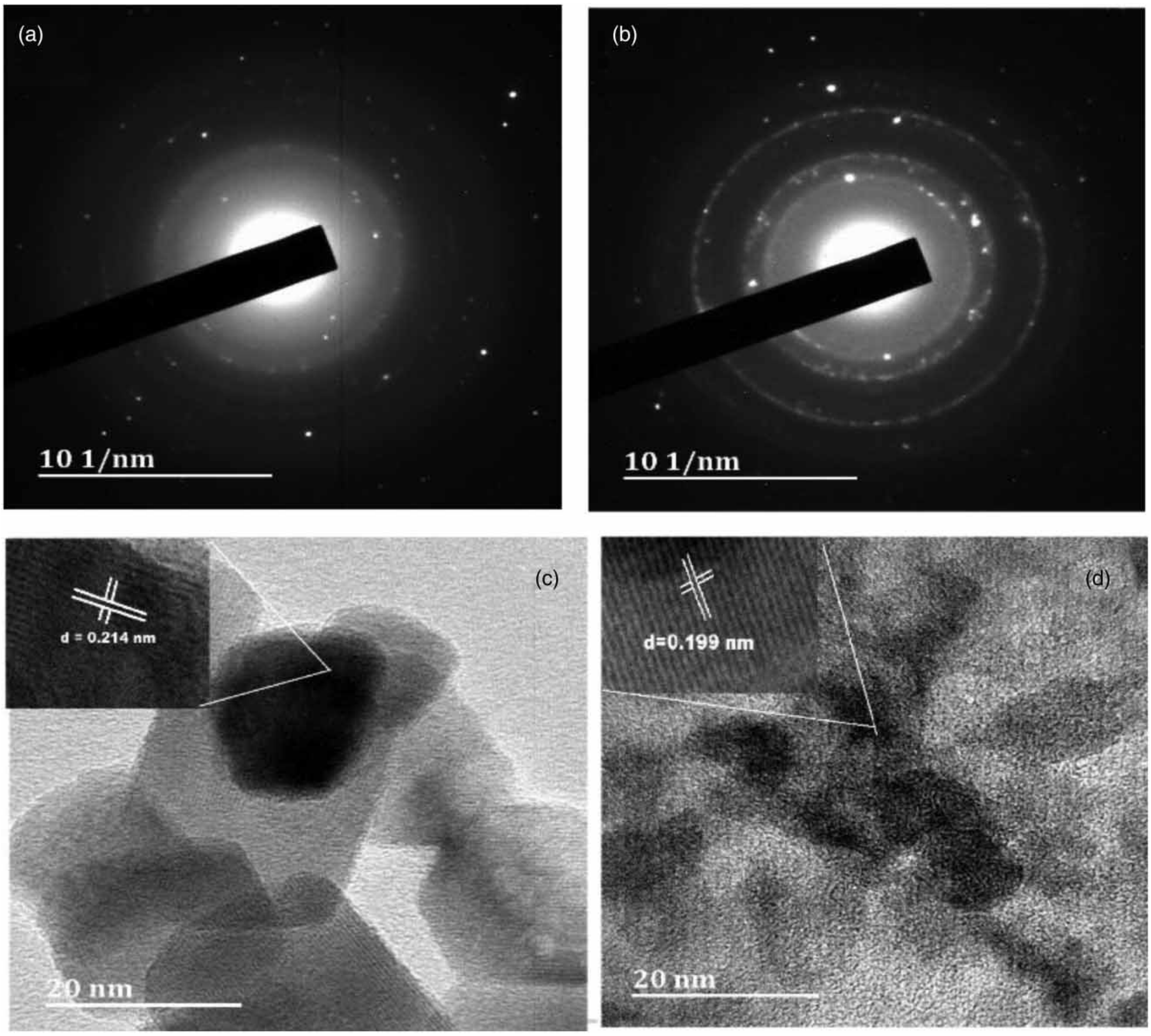

Figure 5 | SAED images of the catalysts (a) ZnO–Co/CCA, (b) ZnO–Ni/CCA, (c) d-spacing of ZnO–Co/CCA, and (d) ZnO–Ni/CCA.

4.3. Optical properties

4.3.1. PL analysis

Figure 6 displays the PL spectra of the samples. The ZnO and Co, Ni-doped-ZnO embedded onto CCA was excited at 3.82 eV (350 nm). The UV emission peak centred at ~397 and 422 nm for the pure ZnO originated from a near-band edge (NBE) emission in the UV region and deep-level defect emission in the visible region, respectively. This results from the recombination of excited electrons from levels located below the conduction band (CB) to the valence band (VB) holes (Ashokkumar & Muthukumaran 2015).

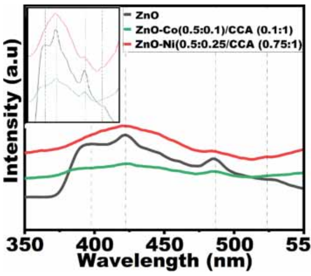

Figure 6 | PL spectra of ZnO and ZnO-M/CCA showing best-performing catalysts.

The ZnO–Co (0.5:0.1)/CCA (0.1:1) and ZnO–Ni (0.5:0.25)/CCA (0.75:1) display peaks at 405 and 412 nm, respectively. This emission peak is reduced in the Co-doped-ZnO/CCA band and intensified in the Ni-doped-ZnO/CCA. Low fluorescence intensity indicates less charge recombination and high separation rates. Perhaps, the increased recombination in the photogenerated excitons in the Ni-doped-ZnO/CCA may be due to overwhelmed separation capability of CCA. In addition, a minimal crystal defect that would have otherwise served as a trap (Salem *et al.* 2013; Gopchandran 2016) for the electrons to enable capture by the CCA but served as a point source of recombination for charges (Rochkind *et al.* 2014), hence the observed increased fluorescence intensity in the ZnO–Ni/CCA.

Furthermore, deep-level defect emission signifies the existence of intrinsic defects in the nanostructures. However, two emission peaks were observed in the blue emission region. As observed from Figure 6, the emission spectra peak in the visible region for all the ZnO-modified nanocatalysts is weak and broad. The peak at 422 nm has been linked to transitions from the bottom of the CB to the O_i levels (Gandhi *et al.* 2014). In contrast, the peak at 486 nm is associated with electronic transitions from the shallow donor (Zn_i) to the shallow acceptor (V_{zn}) levels. The broad, intense green-to-red band emission for undoped ZnO centred at 528 nm is caused by transitions from deep donor levels to the VB caused by oxygen vacancies (V_o). The emission spectra of Co-doped-ZnO/CCA samples are quenched when compared to undoped ZnO under the same excitation conditions, as observed in Figure 6 (Ashokkumar & Muthukumaran 2015).

4.3.2. UV–Vis (diffuse reflectance spectroscopy)

The diffuse reflectance spectra of the metal-doped-ZnO materials (ZnO–Co (0.5:0.1)/CCA (0.1:1) and ZnO–Ni (0.5:0.25)/CCA (0.75:1)) are shown in Supplementary material, Figure S2. The Ni and Co-doped-ZnO showed significant bandgap shifts from 3.21 to 2.65 and 2.59 eV, respectively, i.e. strong absorption in the visible range. These bands are due to d–d transitions of Ni^{+2}/Co^{2+} ions tetrahedrally coordinated (Estévez-Hernández *et al.* 2017). The most plausible reason for the reduction in bandgap is mainly due to the sp-d exchange interaction between the localised d electrons and band electrons of the Ni/Co ions, which are incorporated in the ZnO lattice (He *et al.* 2012a). Furthermore, Figure 7 shows the diffuse reflectance UV spectra of the CCA-supported

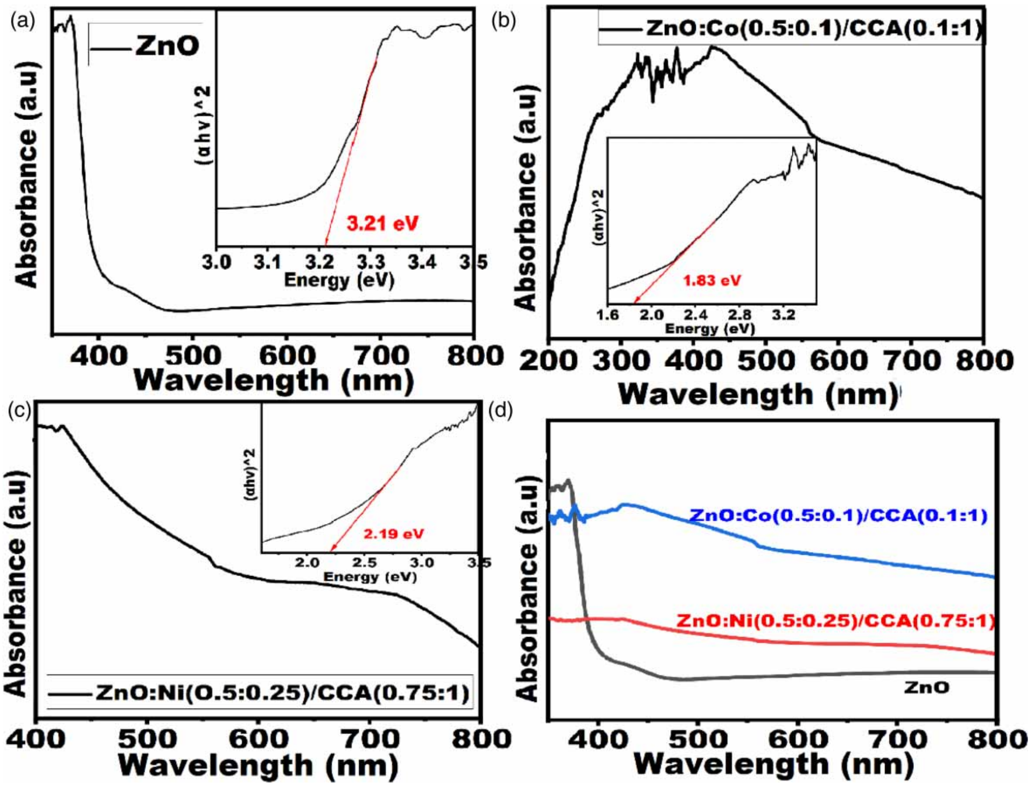

Figure 7 | The UV/Vis absorption of prepared nanoparticles and, as insets, the bandgap estimation UV–Vis spectra of ZnO and CCA-supported metal-doped-ZnO nanoparticle for (a) ZnO, (b) ZnO–Co/CCA, (c) ZnO–Ni/CCA, and (d) the UV/Vis absorption of all prepared nanoparticles, ZnO, ZnO–Co/CCA, and ZnO–Ni/CCA.

Co- and Ni-doped-ZnO and undoped ZnO, indicating that the CCA/metal-ion–doped-ZnO resulted in a significant redshift of the band edge from 386 to 678 nm (Navío *et al.* 1999). This is because a metal-ion-doped-ZnO material has a lower energy level than ZnO. Thus, the nanosized metal colloids exhibited intense absorption in the visible range (Sarmah *et al.* 2018; Tran Thi *et al.* 2019). In addition, the presence of carbon in the CCA supports could be responsible for further shift of the absorption edge to the visible light region (7,168).

The results obtained from the UV–Vis diffuse reflectance were used to estimate the bandgap directly (Figure 7 as insets) (Ravidhas *et al.* 2015). The bandgap of bare ZnO was determined to be 3.21 eV, which is close to the known literature value of 3.37 eV for pure ZnO nanocatalysts. The bandgap energies were significantly reduced when the metal-ion-doped-ZnO catalysts were supported on the CCA. The bandgap of the free ZnO nanoparticles was reduced to 1.83 eV after supporting the materials onto the CCA. The decrease in the bandgap of the CCA-supported catalysts is much more significant than the 0.05 eV decrease reported for carbon-doped-ZnO (Srinivasan *et al.* 2019). The presence of carbon, alumina, and metal ions on the ZnO matrix may have contributed to the catalysts' bandgap narrowing, resulting in an enhanced shift of the band edge towards the visible region of the spectrum (Singh *et al.* 2017).

4.4. Chemical structure

4.4.1. FTIR

FTIR analysis was used to investigate the chemical structure of the as-prepared ZnO, CCA, ZnO–Co (0.5:0.1)/CCA (0.1:1) and ZnOvNi (0.5:0.25)/CCA (0.75:1). The results of the samples were recorded in the range of 400–4,000 cm^{-1}, shown in Supplementary material, Figure S6 and Figure 8. Metal oxides generally exhibit characteristic absorption bands in the IR fingerprint region. As shown in Figure 8, the ZnO spectrum had several distinct peaks. The intensity bands ranging from 1,117 to 1,700 cm^{-1} were due to carbonate moieties on the surface of the ZnO due to CO_2 emission during heat treatment (Kwon *et al.* 2002). Peaks at 1,117 and 1,333 cm^{-1} correspond to C–OH stretching and bending, respectively, while absorptions at 1,459 and 1,647 cm^{-1} are contributed to the stretching modes of the $C=C$ and C–O functional groups, which are associated with residues of acetate ions from the metal precursor salts (Khan *et al.* 2015). The stretching of the OH bond is assigned small broadband at 3,414 cm^{-1}. The characteristic bands at 877 and 692 cm^{-1} are typical for Zn–O(Jayarambabu *et al.* 2015).

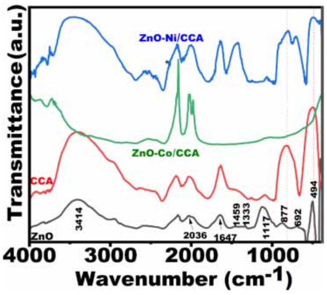

Figure 8 | FTIR spectra of ZnO–CCA, ZnO–Ni/CCA, and ZnO–Co/CCA nanocomposites.

Investigation of the IR peaks below 1,000 cm^{-1} is significant because they indicate the presence or absence of Zn–O bonds and their functional groups. As observed in Figure 8, the shift in vibration frequencies of the ZnO–Co and ZnO–Ni nanoparticles between the 400 and 1,000 cm^{-1} range is caused by the incorporation of nickel/cobalt ions into the ZnO hexagonal wurtzite lattice. A strong absorption band seen in the 400–600 cm^{-1} range is for the Zn–Ni–O or Zn–Co–O stretching frequencies. Although broad absorption is observed in this range for all the samples, the positioning of the peaks varied depending on the Ni/Co-doping. The type of doping species affects the spectra, and it has been observed that the broadening at the shoulder of the ZnO band at 495 cm^{-1} is due to the stretching of M–O peaks ($M=$ Co, Ni, or Zn), which is shifted to 542 cm^{-1} for the ZnO–Ni and 581 cm^{-1} for the ZnO–Co materials. However, the peak at 495 cm^{-1} on ZnO and ZnO–Co/CCA spectra was very weak on ZnO–Ni/CCA (Supplementary material, Figure S7). Perhaps, this observation is due to the low quantity of Ni in the composites (Figure 8). The existence of a shift (blue shift) in frequencies with dopant species

(Ni/Co ions) may be due to changes in bond strength with the replacement of Zn^{2+} with Co^{2+}/Ni^{2+}, confirming the incorporation of Co^{2+}/Ni^{2+} into the ZnO lattice (Shinde *et al.* 2014). In addition, a very weak peak at 2,251 cm^{-1} ('*') was observed on the ZnO–Ni/CCA, corresponding to the $N=C=O$ group. Additionally, the absorption band at 2,000–2,400 cm^{-1} on the CCA and ZnO-M/CCA represents vibrations of oxygen-carrying reactive species (He *et al.* 2012b). It should be noted that the data obtained by XRD, and optical studies support the obtained results.

The typical alumina Al–O–Al band at 670 cm^{-1} (Jun-Cheng *et al.* 2006) was shifted to 821 cm^{-1} on CCA and then to a lower wavenumber of 803 cm^{-1} on the ZnO–Ni/CCA and ZnO–Co/CCA spectra. Furthermore, the band at 1,100 cm^{-1}, which is also typical of alumina due to Al–O vibration mode (Xu *et al.* 2017), was shifted to 1,090 cm^{-1} on the CCA spectrum and 1,065 cm^{-1} on both ZnO–Ni/CCA and ZnO–Co/CCA spectra due to C–O–C vibrational. The absence of the characteristic band (Jun-Cheng *et al.* 2006) associated with alumina between 1,000 and 435 cm^{-1} on the CCA spectrum confirmed the formation of CCA, as observed in Figure 8. Compared to pure alumina, these peaks shifted to higher wavenumbers (redshift). The shift revealed a unique interfacial interaction between alumina and carbon, stabilising the composite. These findings confirmed the alumina-to-CCA transformation.

4.5. Thermal stability

Thermogravimetric analysis (TGA) was used to determine the thermal stability and degree of surface modification. The ZnO, ZnO–Co (0.5:0.1)/CCA (0.1:1) and ZnO–Ni (0.5:0.25)/CCA (0.75:1) nanocomposites underwent four, six, and two stages of weight loss, resulting in 96, 91, and 90% loss of weight, respectively. The removal of physically adsorbed water and some organic components from the ZnO, ZnO–Ni/CCA, and ZnO–Co/CCA nanocomposites resulted in weight losses of 1.59% (100–542 °C), 3.79% (100–150 °C), and 6.17% (100–189 °C) as the first step respectively. The second step involved the removal of physisorbed and chemisorbed carbon materials resulting in weight losses of 1.39% (542–714 °C), 1.56% (142–244 °C), and 6.17% for ZnO, ZnO–Ni/CCA, and ZnO–Co/CCA, respectively. For the ZnO sample, the third step was more of a continuation of the second step of 0.21% (714–784 °C) weight loss due to physisorbed and chemisorbed carbon materials, and then the final step, which was a rapid 0.35% (from 784 °C) due to complete removal of organic materials. While for the ZnO–Co/CCA, the second step was the final weight loss of about 4% (from 190 °C).

The third step, 0.84% (244–440 °C) to the fourth step, 0.78% (440–581 °C) weight losses for ZnO–Ni/CCA are due to physisorbed and chemisorbed carbon materials. The fifth and final weight losses of 1.73 and 0.35% (581 °C and above) are due to the complete removal of organic materials (Supplementary material, Figure S4).

4.6. EIS studies

Charge transport across a photocatalytic semiconductor and charge transfer across the interface of its surface to the adsorbed species play essential roles in semiconductor-photocatalysis. Solid-state EIS is a vital tool for studying the electrical properties of semiconductor materials. All the prepared samples displayed a semi-circle component at a high frequency with a diameter corresponding to the transfer resistance (R_{ct}–) and a linear component at a high frequency (Begum *et al.* 2017; Gul *et al.* 2019; Merlo *et al.* 2021).

Figure 9 displays the Nyquist graphs of the prepared samples [ZnO, ZnO–Co (0.5:0.1)/CCA (0.1:1) and ZnO–Ni (0.5:0.25)/CCA (0.75:1)].

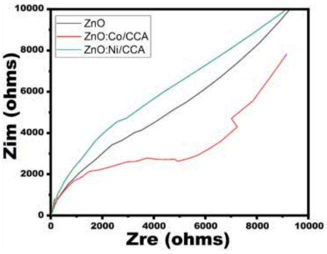

Figure 9 | Nyquist plots for ZnO and metal-doped-ZnO implanted onto CCA in Na_2SO_4 solutions.

The ZnO–Co/CCA composite displayed the smallest diameter (incomplete circle), indicating that it had the best conductivity (smallest transfer resistance) compared to ZnO or ZnO–Ni/CCA. The most credible reason for this may be that CCA acts as an electron sensitiser due to its surface's variety of reactive groups (Mahlambi *et al.* 2014; Tonda *et al.* 2014; Liu *et al.* 2019).

4.7. Photocatalytic activity

The catalysts were utilised under visible light working conditions in the photodegradation of the chosen pollutants. The CR and MO azo dyes were used as model pollutants in the set-up at 20 mg L^{-1} concentrations. Figure 10 illustrates the adsorption–degradation profiles, while Figure 11 displays the UV–Vis absorption spectra of the CR and MO dyes ($\lambda_{max} = 498$ and 465) nm for the degradation in the presence of the Co/Ni-doped-ZnO/CCA catalysts (insets are the colour changes from initial at $t = 0$ min to the final $t = 180$ min).

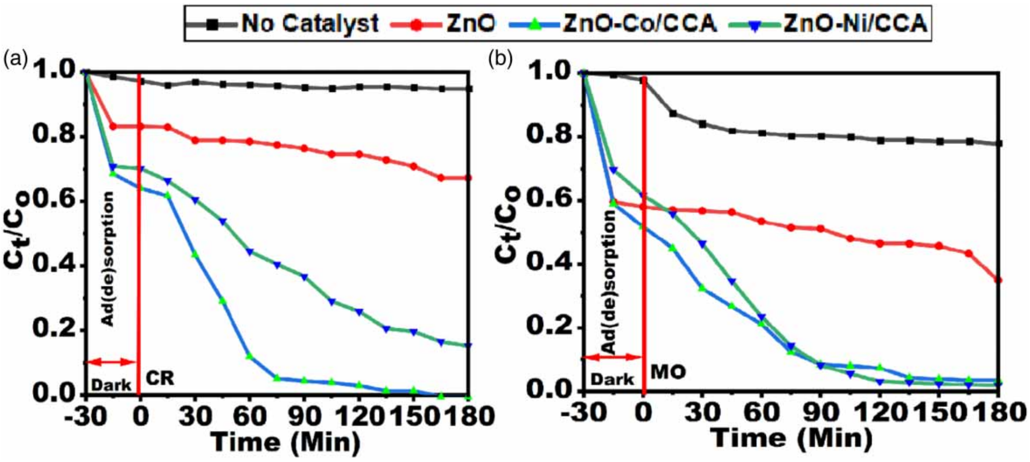

Figure 10 | Photocatalytic performance of (a, b) ZnO and metal-doped-ZnO embedded onto CCA against CR and MO dyes with and without a catalyst (photolysis).

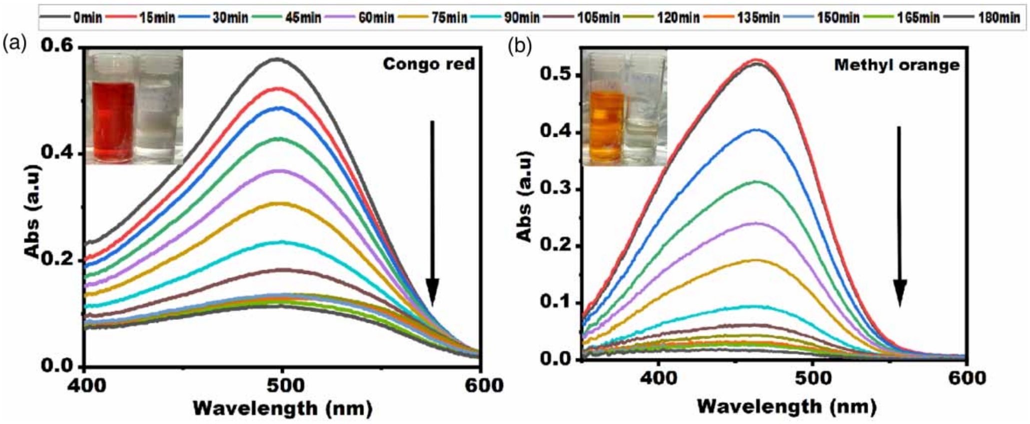

Figure 11 | UV/Vis absorbance of (a) Congo red and (b) methyl orange as a function of time during photocatalysis using the best catalyst: ZnO–Co (0.5:0.1)/CCA (0.1:1) (inset: colour before and after degradation). Please refer to the online version of this paper to see this figure in colour: https://dx.doi.org/10.2166/wpt.2023.123.

In the experiment, the suspension of nanocatalyst and dye was shaken in a dark enclosure for 30 min before irradiation by visible light. It is important to note that the ZnO–Co (0.5:0.1)/CCA (0.1:1) and ZnO–Ni (0.5:0.25)/CCA (0.75:1) samples showed higher adsorption of the dyes than pure ZnO.

The data presented in Figures 10(a) and 10(b) illustrate the superior catalytic performance of the modified ZnO catalyst due to larger specific active areas and hence more reactive sites. All the (ZnO-M/CCA) were effective in the removal of the dyes. Also, the CCA must be present in a critical quantity to ensure the optimum light-harvesting capacity of the support. Overly large amounts of the catalyst block the CCA's pores and reduce its performance (Huang *et al.* 2014). This is due to the metal-doped-ZnO catalyst being locked into the CCA pores (Lin *et al.* 2019; Solodovnichenko *et al.* 2019).

The adsorption of the dye molecules to the reactive surface of the catalyst is critical for effective photocatalysis. The results showed photolysis of 5% for the CR and 22% for the MO azo dyes. Adsorption (in the dark) removed 17, 36, and 30% of CR over ZnO, ZnO–Co/CCA and ZnO–Ni/CCA, respectively. Similarly, adsorption without photolysis removed 42, 38, and 48% of MO over ZnO, ZnO–Co/CCA, and ZnO–Ni/CCA, respectively. The observed absorptive capacity is in close agreement with the BET data discussed in Section 4.1.2. The amount of dye adsorbed is due to the high specific surface areas of the prepared catalyst (Table 2). In addition, these findings suggest that visible light and a photocatalyst are required for complete pollutant dye destruction to be effective. In addition, the data presented in Figure 10(a) and 10(b) shows that the ZnO–Co/CCA photocatalyst degraded 100% of the CR in 150 min and 97% of the MO dye in 180 min. Similarly, the ZnO–Ni/CCA degraded 85% of CR and 98% of MO. The results confirmed that complete dye removal occurs via a photocatalytic pathway involving the prepared ZnO-M/CCA catalyst.

The excellent photocatalytic performance of the ZnO-M/CCA material is attributable to many factors, including the CCA, which caused structural defects that changed the property of ZnO (reduced bandgap energy), thereby increasing light absorption (Srinivasan *et al.* 2019). Furthermore, as shown in Figure 6, photogenerated charge carrier recombination is almost completely suppressed in ZnO–Co/CCA, resulting in its high photoactivity. Similarly, despite increased recombination of the photogenerated excitons, the photocatalytic performance of the ZnO–Ni/CCA is far better than pure ZnO. The increased photocatalytic performance could also be attributed to the prepared material's increased specific area of about 213.93 and 152.37 m^2g^{-1} for ZnO–Co/CCA and ZnO–Ni/CCA, respectively, which increased the number of active sites, combined with enhanced visible light absorption. However, it should be noted that while increased surface area is important for photoactivity, other factors, such as the light-gathering ability of the composite (due to reactive groups Sapkota *et al.* 2019 on CCA) and suppression of the photo-induced charge carrier due to metal doping are also crucial for photocatalytic performance (Nenavathu *et al.* 2018; Praveen *et al.* 2018). Table 2 compares the photocatalytic activities of the as-prepared nanocomposites to related works with a comparable support material reported in the literature.

4.8. Photocatalytic reaction kinetics

To better understand the removal of the model pollutants, a kinetic study (Skinner *et al.* 2020) of the photodegradation of CR and MO by the prepared composites and photolysis was performed (Wu *et al.* 2019). The pseudo-first-order reaction (Equation (5)) was used:

$$\ln\left(\frac{At}{Ao}\right) = -k\mathrm{t} \tag{5}$$

where A_{o} is the initial absorbance of the dyes, A_t is the absorbance of dye at a given time t after exposure to visible light, k is the pseudo-first-order rate constant, and t is the time in minutes. As presented, Supplementary material, Figure S7 displays the line of best fit of ln (A_t/A_o) as a function of time.

The gradient of each plot and the rate constants k for the removal of CR by ZnO, ZnO–Ni/CCA, and ZnO–Co – Co/CCA catalysts are 0.0014, 0.0088, and 0.027 min^{-1}, respectively. While the rate constants for removing MO by ZnO, ZnO–Ni/CCA and ZnO–Co/CCA catalysts are 0.0029, 0.0169, and 0.0022 min^{-1}, respectively. These results are consistent with data reported for the ZnO catalyst (Wu *et al.* 2019).

The rate constants for the photolysis of CR and MO are very low, with values of 0.0002 and 0.0019 min^{-1}, respectively. ZnO–Co/CCA, photodegradation of CR and MO, is 20 and seven times faster than with bare ZnO. Also, the photolysis of CR and MO by degradation using ZnO–Co/CCA are 141 and 12 times faster. These remarkable results are attributed to the lowest bandgap exhibited by ZnO–Co/CCA, as shown in Figure 7(b). Perhaps, the efficient suppression of the recombination of the photo-induced charge carrier due to the metal doping, coupled with the larger active area, are responsible for the observed catalytic properties. Accordingly, embedding the metal-doped-ZnO onto CCA causes a fundamental alteration of the material's electronic band structure, resulting in improved performance. More importantly, the carbon coating due to the CCA allowed for cross-plane movement (diffusion channels), which improved charge and mass transfer and increased photocatalytic efficiency (Li *et al.* 2020; Lu *et al.* 2020). The kinetics data of the photocatalytic degradation of the model dyes are displayed in Table 3.

Table 3 | Observed pseudo-first-order rate constants (*k*), maximum degradation (%), and the photolysis of dyes, pristine ZnO, and ZnO-M/CCA nanocomposites

Catalyst	*k* (min^{-1}) CR (MO)	Maximum degradation (%) CR (MO)
Dye (No catalyst)	0.0002 (0.0019)	5 (39)
ZnO	0.0014 (0.0029)	33 (65)
ZnO–Ni/CCA	0.0088 (0.0169)	84 (97)
ZnO–Co/CCA	0.0268 (0.0022)	100 (98)

Charge scavenging experiments were conducted to identify the reactive entities responsible for dye removal by the ZnO-M/CCA photocatalysts. Scavengers for photo-induced $^{\cdot}OH$, h^+, and $O_2^{\cdot -}$ were introduced in the form of IPA, disodium ethylenediaminetetraacetic acid (EDTA), and *p*- BQ. The scavenger solutions significantly reduced the photodegradation of the model pollutants by ZnO-M/CCA. In Figures 12(a) and 12(b), the dyes were photodegraded at the highest values without the scavengers. Among the scavengers, the removal rate decreased in the following order: (a) for CR, EDTA < IPA < BQ and (b) for MO, BQ < EDTA < IPA. As a result, it was clear that $O_2^{\cdot -}$ was more energetically involved in the photodegradation of MO, followed by h^+ and $^{\cdot}OH$. Similarly, the most active radical in CR is h^+, followed by OH and $O_2^{\cdot -}$.

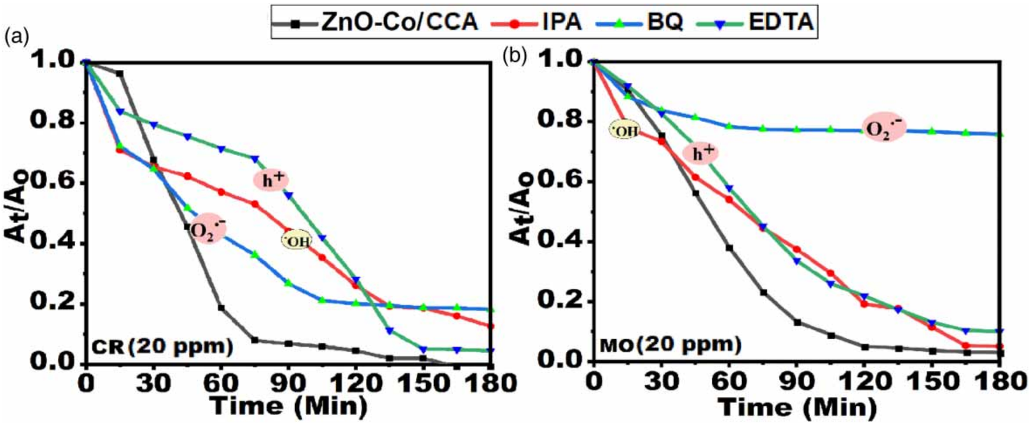

Figure 12 | (a, b) Degradation of CR and MO by Co-doped-ZnO embedded onto CCA samples with and without scavengers.

The main factors responsible for the catalysts' improved removal performance are enhanced light absorption, the pollutant adsorption capacity of the nanocomposite, and suppression of recombination exciton through efficient separation. This prepared catalyst met these requirements. In general, UV is the only way to stimulate ZnO. However, some factors provide visible light absorbance (Baruah *et al.* 2010; Bouarroudj *et al.* 2021; Senasu *et al.* 2021).

Based on the results obtained from Figure 12, a plausible photocatalytic mechanism of removal of tested dyes by ZnO-M/CCA is suggested in Figure 13.

The exciton electron–hole (e^-/h^+) pair produced during photocatalysis is prone to irradiative recombination, which must be hindered to make available the electron for further dye degradation reactions. The photo-induced charged pair recombination is successfully hindered if they are separated efficiently for long periods. In the illustrations shown in Figure 13, when the catalyst system was exposed to visible light irradiation, the electron in the VB of the main semiconductor ZnO is agitated and stimulated to the CB, where it is quickly captured by CCA, while the h^+ fragment remains in the VB. For the Co/Ni-doped-ZnO/CCA, the Co/Ni dopants trap the photoexcited electrons from the ZnO CB before capturing by CCA, while h^+ remained in the VB, limiting electron–hole recombination in these catalysts.

Therefore, the superior photocatalytic performance of ZnO-M/CCA may be attributed to the dual ease of generation of photo-charges (due to the low bandgap energy) and reduced exciton recombination.

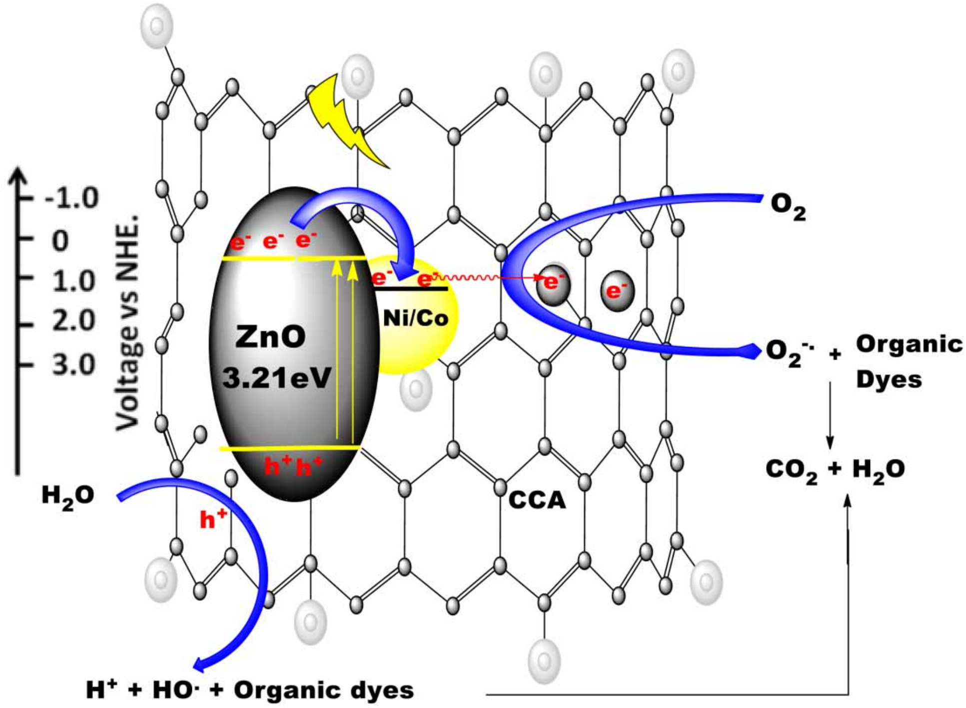

Figure 13 | Possible photocatalytic mechanism of ZnO–metal/CCA nanocomposite under visible light irradiation.

4.9. Degradation analysis

Many variables were monitored during the wastewater cleaning process, including pH, colour, COD, and total dissolved solids (TDS). The effect of pollution on these parameters reveals the level of contamination. Physico-chemical analyses are necessary during the photocatalytic removal of pollutant dyes. Inspection of the untreated CR and MO dye solutions revealed characteristic red/pinkish and yellow colours. When the MO and CR dyes were treated with the ZnO–Co (0.5:0.1)/CCA (0.1:1) and ZnO–Ni (0.5:0.25)/CCA (0.75:1) catalyst, their colour changed to light pink and clear solution, respectively. The extent of COD reductions and other data obtained in this study are presented in Table 4.

Table 4 | Physicochemical parameters

Entry	Catalyst	Colour	Average TDS (ppm)	pH	Average COD reduction (%)
1	MO	Yellow	85.3	7.16	–
2	CR	Red	144.9	5.52	–
3	ZnO	Whitish/Clear	363 (229.7)[a]	7.16 (5.90)[a]	26 (37)[a]
4	ZnO–Co –Co/CCA	Pink/Clear	135.9 (77.1)[a]	7.20 (7.90)[a]	65 (80)[a]

[a] MO (CR).

After 180 min of visible light exposure with bare ZnO and ZnO–Co/CCA, the COD for MO was reduced by 37% (entry 3) and 80% (entry 4), respectively. For CR, the COD reduction for bare ZnO and ZnO–Co/CCA was 26% (to 39 mg) and 65% (to 19 mg/L), respectively. This could be because intermediate products are more difficult to degrade and oxidise more slowly than the dyes (Ince *et al.* 1997; Bilinska *et al.* 2015; Nagarajan & Venkatanarasimhan 2019). The results confirmed the ZnO–Co/CCA system's higher mineralisation potential for dye removal from the wastewater. As evidenced by an increase in the TDS value 229.7(363) [MO (CR)-entry 3], the presence of ZnO nanoparticles may be responsible for the whitish appearance of the cleaned water. TDS analysis revealed an increase in the number of solid particles in aqueous solutions, which measures how much nanocatalyst was retained. When ZnO–Co/CCA nanocatalysts were used, TDS increased by 21% for MO and 11% for CR, compared to bare ZnO, which increased by 169 and 151%, respectively. This demonstrated the catalyst support's effectiveness in reducing catalyst leaching into the treated water. Based on the TDS and COD study, it is clear that the fabricated catalysts were very effective in decolourising and decontaminating the wastewater. The COD results closely match those of the photodegradation analysis. Thus, indicating that the pollutant dyes were effectively mineralised into harmless water.

4.10. Reusability of nanocomposite/photostability

The photostability of the ZnO–Co/CCA, the most active catalyst, was further investigated, and the results are presented in Figure 14. In the experiment, the suspension of nanocatalyst and dye was shaken in a dark enclosure for 30 min before irradiation by visible light.

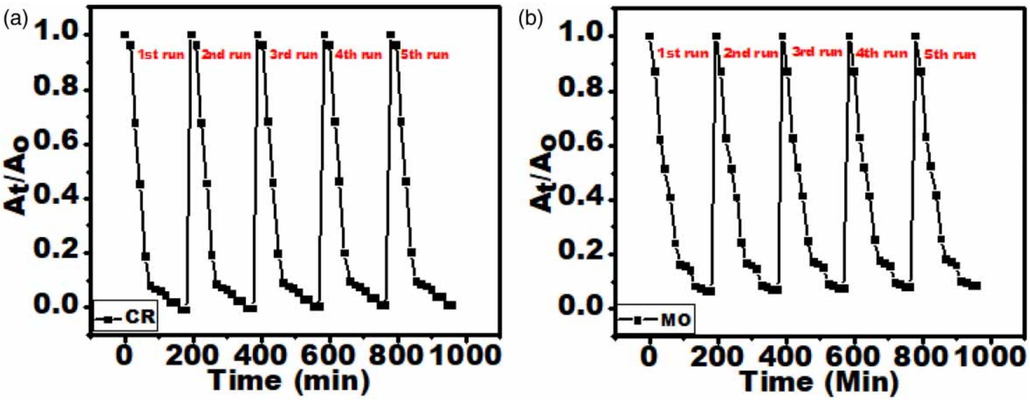

Figure 14 | Reusability of the ZnO–Co/CCA catalyst for degrading CR (a) and MO (b).

After each run, the catalyst material was retrieved by centrifugation and filtered, rinsed severally with deionised water, dried overnight at 80 °C, and ready for the next cycle. The test showed little or no loss in catalyst performance by the fifth cycle. There was only a one-point decrease in dye removal efficiency from 100% in the first cycle to 99% in the fifth cycle towards CR removal. Similarly, the photocatalytic performance of MO decreased from 98 to 96% by the fifth cycle [Figure 14(a) and 14(b)]. Thus, attesting to the catalyst's high reusability and stability.

5. CONCLUSION

Metal-ion-doped-ZnO nanocatalysts with high visible light photocatalytic activity were successfully implanted on CCA supports. These were applied to the photodegradation of CR and MO dyes, where all the materials displayed high photocatalytic activities. The CCA-supported version maintained its crystallinity and catalytic effectiveness, directly correlated to its better performance than the unsupported bare metal-ion-doped-ZnO and pure ZnO variants. This effectiveness may be connected to enhanced surface area and pore volume due to the support. The presence of CCA helps to reduce the recombination of excitons and increase the active site, thus improving the overall photocatalytic performance of the composites. Based on the obtained results, it is concluded that, for the first time, highly active metal-ion-doped-ZnO catalysts have been synthesised and incorporated onto CCA supports for the visible light photodegradation of azo dyes. This is a significant step forward in using visible light for wastewater remediation through ZnO-driven materials.

ACKNOWLEDGEMENT

We thank ESKOM (TESP programme) and the National Research Foundation of South Africa for financial support.

ETHICAL APPROVAL

The work reported in this paper does not require any ethical approval.

DATA AVAILABILITY STATEMENT

All relevant data are included in the paper or its Supplementary Information.

CONFLICT OF INTEREST

The authors declare there is no conflict.

REFERENCES

Ajmal, A., Majeed, I., Malik, R. N., Idriss, H. & Nadeem, M. A. 2014 Principles and mechanisms of photocatalytic dye degradation on TiO_2 based photocatalysts: A comparative overview. *Rsc Advances* **4**(70), 37003–37026. https://doi.org/10.1039/C4RA06658H.

Anwer, H., Mahmood, A., Lee, J., Kim, K. H., Park, J. W. & Yip, A. C. 2019 Photocatalysts for degradation of dyes in industrial effluents: Opportunities and challenges. *Nano Research* **12**, 955–972. https://doi.org/10.1007/s12274-019-2287-0.

Aruna devi, R., Kavitha, B., Rajarajan, M. & Suganthi, A. 2018 An eco-friendly highly stable and efficient Ni-CS codoped wurtzite ZnO nanoplate: A smart photocatalyst for the quick removal of food dye under solar light irradiation. *Separation Science and Technology* **53**(15), 2456–2467. https://doi.org/10.1080/01496395.2018.1447582.

Ashokkumar, M. & Muthukumaran, S. 2015 Electrical, dielectric, photoluminescence and magnetic properties of ZnO nanoparticles co-doped with Co and Cu. *Journal of Magnetism and Magnetic Materials* **374**, 61–66. https://doi.org/10.1016/j.jmmm.2014.08.023.

Baruah, S., Mahmood, M. A., Myint, M. T. Z., Bora, T. & Dutta, J. 2010 Enhanced visible light photocatalysis through fast crystallization of zinc oxide nanorods. *Beilstein Journal of Nanotechnology* **1**(1), 14–20. https://doi.org/10.3762/bjnano.1.3.

Begum, H., Ahmed, M. S. & Jeon, S. 2017 New approach for porous chitosan–graphene matrix preparation through enhanced amidation for synergic detection of dopamine and uric acid. *ACS Omega* **2**(6), 3043–3054. https://doi.org/10.1021/acsomega.7b00331.

Behnajady, M. A., Modirshahla, N. & Ghazalian, E. 2011 Synthesis of ZnO nanoparticles at different conditions: a comparison of photocatalytic activity. *Digest Journal of Nanomaterials and Biostructures* **6**(1), 467–474.

Bekele, B., Jule, L. T. & Saka, A. 2021 The effects of annealing temperature on size, shape, structure and optical properties of synthesized zinc oxide nanoparticles by sol-gel methods. *Digest Journal of Nanomaterials & Biostructures* **16**(2), 471–478.

Bilinska, L., Gmurek, M. & Ledakowicz, S. 2015 Application of advanced oxidation technologies for decolorization and mineralization of textile wastewaters. *Journal of Advanced Oxidation Technologies* **18**(2), 185–194. https://doi.org/10.1515/jaots-2015-0202.

Błachnio, M., Staszczuk, P., Grodzicka, G., Lin, L. & Zhu, Y. 2007 Adsorption and porosity properties of carbon-covered alumina surfaces. *Journal of Thermal Analysis and Calorimetry* **88**(2), 601–606. https://doi.org/10.1007/s10973-006-8067-3.

Blake, D. M. 1994 *Bibliography of Work on the Photocatalytic Removal of Hazardous Compounds From Water and air (No. NREL/TP-430-6084)*. National Renewable Energy Lab., Golden, CO, United States. https://doi.org/10.2172/12101.

Bouarroudj, T., Aoudjit, L., Djahida, L., Zaidi, B., Ouraghi, M., Zioui, D., Mahidine, S., Shekhar, C. & Bachari, K. 2021 Photodegradation of tartrazine dye favored by natural sunlight on pure and (Ce, Ag) co-doped ZnO catalysts. *Water Science and Technology* **83**(9), 2118–2134. https://doi.org/10.2166/wst.2021.106.

Chai, C., Liu, H. & Yu, W. 2021 The electronic and optical properties of the Fe, Co, Ni and Cu doped ZnO monolayer photocatalyst. *Chemical Physics Letters* **778**, 138765. https://doi.org/10.1016/j.cplett.2021.138765.

Chen, X., Wu, Z., Liu, D. & Gao, Z. 2017 Preparation of ZnO photocatalyst for the efficient and rapid photocatalytic degradation of azo dyes. *Nanoscale Research Letters* **12**, 1–10. https://doi.org/10.1186/s11671-017-1904-4.

Değermenci, G. D., Değermenci, N., Ayvaoğlu, V., Durmaz, E., Çakır, D. & Akan, E. 2019 Adsorption of reactive dyes on lignocellulosic waste; characterization, equilibrium, kinetic and thermodynamic studies. *Journal of Cleaner Production* **225**, 1220–1229. https://doi.org/10.1016/j.jclepro.2019.03.260.

Dickhout, J. M., Moreno, J., Biesheuvel, P. M., Boels, L., Lammertink, R. G. H. & De Vos, W. M. 2017 Produced water treatment by membranes: a review from a colloidal perspective. *Journal of Colloid and Interface Science* **487**, 523–534. https://doi.org/10.1016/j.jcis.2016.10.013.

Dodd, A. C., McKinley, A. J., Saunders, M. & Tsuzuki, T. 2006 Effect of particle size on the photocatalytic activity of nanoparticulate zinc oxide. *Journal of Nanoparticle Research* **8**, 43–51. https://doi.org/10.1007/s11051-005-5131-z.

Estévez-Hernández, O., Hernández, M. P., Farías, M. H., Rodríguez-Hernández, J., Gonzalez, M. M. & Reguera, E. 2017 Effect of co-doping on the structural, electronic and magnetic properties of $Co_xZn_{1-x}O$ nanoparticles. *Materials Focus* **6**(4), 371–381. https://doi.org/10.1166/mat.2017.1424.

Fenoll, J., Ruiz, E., Hellín, P., Flores, P. & Navarro, S. 2011 Heterogeneous photocatalytic oxidation of cyprodinil and fludioxonil in leaching water under solar irradiation. *Chemosphere* **85**(8), 1262–1268.

Fu, Y. & Viraraghavan, T. 2001 Fungal decolorization of dye wastewaters: A review. *Bioresource Technology* **79**(3), 251–262. https://doi.org/10.1016/S0960-8524(01)00028-1.

Gandhi, V., Ganesan, R., Abdulrahman Syedahamed, H. H. & Thaiyan, M. 2014 Effect of cobalt doping on structural, optical, and magnetic properties of ZnO nanoparticles synthesized by coprecipitation method. *The Journal of Physical Chemistry C* **118**(18), 9715–9725. https://doi.org/10.1021/jp411848t.

Ganesh, R., Boardman, G. D. & Michelsen, D. 1994 Fate of azo dyes in sludges. *Water Research* **28**(6), 1367–1376. https://doi.org/10.1016/0043-1354(94)90303-4.

Ghosh, S. S., Choubey, C. & Sil, A. 2019 Photocatalytic response of Fe, Co, Ni doped ZnO based diluted magnetic semiconductors for spintronics applications. *Superlattices and Microt* **125**, 271–280. https://doi.org/10.1016/j.spmi.2018.10.028.

Goktas, A., Modanlı, S., Tumbul, A. & Kilic, A. 2022 Facile synthesis and characterization of ZnO, ZnO: Co, and ZnO/ZnO: Co nano rod-like homojunction thin films: Role of crystallite/grain size and microstrain in photocatalytic performance. *Journal of Alloys and Compounds* **893**, 162334. https://doi.org/10.1016/j.jallcom.2021.162334.

Gopchandran, R. R. K. 2016 ZnO nanostructures with tunable visible luminescence: Effects of kinetics of chemical reduction and annealing. https://doi.org/10.1016/j.jsamd.2017.02.002.

Gul, H., Shah, A. U. H. A. & Bilal, S. 2019 Achieving ultrahigh cycling stability and extended potential window for supercapacitors through asymmetric combination of conductive polymer nanocomposite and activated carbon. *Polymers* **11**(10), 1678. https://doi.org/10.3390/polym11101678.

He, R., Hocking, R. K. & Tsuzuki, T. 2012a Co-doped ZnO nanopowders: location of cobalt and reduction in photocatalytic activity. *Materials Chemistry and Physics* **132**(2–3), 1035–1040. https://doi.org/10.1016/j.matchemphys.2011.12.061.

He, Y., Zhang, X., Zhang, X., Huang, H., Chang, J. & Chen, H. 2012b Structural investigations of toluene diisocyanate (TDI) and trimethylolpropane (TMP)-based polyurethane prepolymer. *Journal of Industrial and Engineering Chemistry* **18**(5), 1620–1627. https://doi.org/10.1016/j.jiec.2012.02.023.

Huang, Z. F., Pan, L., Zou, J. J., Zhang, X. & Wang, L. 2014 Nanostructured bismuth vanadate-based materials for solar-energy-driven water oxidation: A review on recent progress. *Nanoscale* **6**(23), 14044–14063. https://doi.org 10.1039/C4NR05245E.

Ince, N. H., Stefan, M. I. & Bolton, J. R. 1997 UV/H_2O_2 degradation and toxicity reduction of textile azo dyes: Remazol Black-B, a case study. *Journal of Advanced Oxidation Technologies* **2**(3), 442–448. https://doi.org/10.1515/jaots-1997-0312.

Jayarambabu, N., Kumari, B. S., Rao, K. V. & Prabhu, Y. T. 2015 Beneficial role of zinc oxide nanoparticles on green crop production. *International Journal of Multidisciplinary Advanced Research Trends* **2**, 273–282.

Jun-Cheng, L., Lan, X., Feng, X., Zhan-Wen, W. & Fei, W. 2006 Effect of hydrothermal treatment on the acidity distribution of γ-Al_2O_3 support. *Applied Surface Science* **253**(2), 766–770. https://doi.org/10.1016/j.apsusc.2006.01.003.

Kalita, A. & Kalita, M. P. 2017 Williamson-Hall analysis and optical properties of small sized ZnO nanocrystals. *Physica E: Low-Dimensional Systems and Nanostructures* **92**, 36–40. https://doi.org/10.1016/j.physe.2017.05.006.

Kazakova, M. A., Vatutina, Y. V., Prosvirin, I. P., Gerasimov, E. Y., Shuvaev, A. V., Klimov, O. V., Noskov, A. S. & Kazakov, M. O. 2021 Boosting hydrodesulfurization activity of CoMo/Al2O3 catalyst via selective graphitization of alumina surface. *Microporous and Mesoporous Materials* **317**, 111008. https://doi.org/10.1016/j.micromeso.2021.111008.

Khan, M., Naqvi, A. H. & Ahmad, M. 2015 Comparative study of the cytotoxic and genotoxic potentials of zinc oxide and titanium dioxide nanoparticles. *Toxicology Reports* **2**, 765–774. https://doi.org/10.1016/j.toxrep.2015.02.004.

Kwon, Y. J., Kim, K. H., Lim, C. S. & Shim, K. B. 2002 Characterization of ZnO nanopowders by the polymerized complex method via an organochemical route. *Journal of Ceramic Processing Research* **3**(3/2), 146–149.

Landers, J., Gor, G. Y. & Neimark, A. V. 2013 Density functional theory methods for characterization of porous materials. *Colloids and Surfaces A: Physicochemical and Engineering Aspects* **437**, 3–32. https://doi.org/10.1016/j.colsurfa.2013.01.007.

Li, M., Wu, G., Liu, Z., Xi, X., Xia, Y., Ning, J., Yang, D. & Dong, A. 2020 Uniformly coating ZnAl layered double oxide nanosheets with ultra-thin carbon by ligand and phase transformation for enhanced adsorption of anionic pollutants. *Journal of Hazardous Materials* **397**, 122766. https://doi.org/10.1016/j.jhazmat.2020.122766.

Lin, L., Lin, W., Zhu, Y. X., Zhao, B. Y., Xie, Y. C., Jia, G. Q. & Li, C. 2005 Uniformly carbon-covered alumina and its surface characteristics. *Langmuir* **21**(11), 5040–5046. https://doi.org/10.1021/la047097d.

Lin, B., Heng, L., Yin, H., Fang, B., Ni, J., Wang, X., Lin, J. & Jiang, L. 2019 Effects of using carbon-coated alumina as support for Ba-promoted Ru catalyst in ammonia synthesis. *Industrial & Engineering Chemistry Research* **58**(24), 10285–10295. https://doi.org/10.1021/acs.iecr.9b01610.

Liu, Y. J. 2011 Characterization of spent catalysts during hydrodemetallization of atmosphere residue. *Advanced Materials Research* **236**, 538–542. Trans Tech Publications Ltd. https://doi.org/10.4028/www.scientific.net/AMR.236-238.538.

Liu, X., Li, W., Chen, N., Xing, X., Dong, C. & Wang, Y. 2015 Ag–ZnO heterostructure nanoparticles with plasmon-enhanced catalytic degradation for Congo red under visible light. *RSC Advances* **5**(43), 34456–34465. https://doi.org/10.1039/C5RA03143E.

Liu, C., Bao, L., Yang, M., Zhang, S., Zhou, M., Tang, B., Wang, B., Liu, Y., Zhang, Z. L., Zhang, B. & Pang, D. W. 2019 Surface sensitive photoluminescence of carbon nanodots: Coupling between the carbonyl group and π-electron system. *The Journal of Physical Chemistry Letters* **10**(13), 3621–3629. https://doi.org/10.1021/acs.jpclett.9b01339.

Lonkar, S. P., Pillai, V. V. & Alhassan, S. M. 2018 Facile and scalable production of heterostructured ZnS-ZnO/Graphene nano-photocatalysts for environmental remediation. *Scientific Reports* **8**(1), 13401. https://doi.org/10.1038/s41598-018-31539-7.

Loo, W. W., Pang, Y. L., Wong, K. H., Lim, S. & Mah, S. K. 2018 Adsorption-photocatalysis of organic dyes using empty fruit bunch activated carbon-metal oxide photocatalyst. In *IOP Conference Series: Materials Science and Engineering*, Vol. 458(1). IOP Publishing, p. 012042. https://doi.org/10.1088/1757-899X/458/1/012042.

Lu, K., Li, B., Zhan, X., Xia, F., Dahunsi, O. J., Gao, S., Reed, D. M., Sprenkle, V. L., Li, G. & Cheng, Y. 2020 Elastic Na x MoS_2-carbon-BASE triple interface direct robust solid–solid interface for all-solid-state Na–S batteries. *Nano Letters* **20**(9), 6837–6844. https://doi.org/10.1021/acs.nanolett.0c02871.

Mahlambi, M. M., Mishra, A. K., Mishra, S. B., Krause, R. W., Mamba, B. B. & Raichur, A. M. 2013 Effect of metal ions (Ag, Co, Ni, and Pd) on the visible light degradation of Rhodamine B by carbon-covered alumina-supported TiO_2 in aqueous solutions. *Industrial & Engineering Chemistry Research* **52**(5), 1783–1794. https://doi.org/10.1021/ie3025505.

Mahlambi, M. M., Mishra, A. K., Mishra, S. B., Krause, R. W., Mamba, B. B. & Raichur, A. M. 2014 Synthesis and characterization of carbon-covered alumina (CCA) supported TiO2 nanocatalysts with enhanced visible light photodegradation of Rhodamine B. In: *Nanotechnology for Sustainable Development 89–99*. Springer International Publishing. https://doi.org/10.1007/s11051-012-0790-z.

Maity, S. K., Flores, L., Ancheyta, J. & Fukuyama, H. 2009 Carbon-modified alumina and alumina−carbon-supported hydrotreating catalysts. *Industrial & Engineering Chemistry Research* **48**(3), 1190–1195. https://doi.org/10.1021/ie800606p.

Manjunatha, C., Abhishek, B., Shivaraj, B. W., Ashoka, S., Shashank, M. & Nagaraju, G. 2020 Engineering the M x Zn 1−x O (M = Al^{3+}, Fe^{3+}, Cr^{3+}) nanoparticles for visible light-assisted catalytic mineralization of methylene blue dye using Taguchi design. *Chemical Papers* **74**, 2719–2731. https://doi.org/10.1007/s11696-020-01113-5.

Masthan, S. K., Prasad, P. S., Rao, K. R. & Rao, P. K. 1991 Hysteresis during ammonia synthesis over promoted ruthenium catalysts supported on carbon-covered alumina. *J Mole Catal* **67**, L1–L5. https://doi.org/10.1016/0304-5102(91)85040-9.

Mendes, F. L., da Silva, V. T., Pacheco, M. E., de Rezende Pinho, A. & Henriques, C. A. 2020 Hydrotreating of fast pyrolysis oil: A comparison of carbons and carbon-covered alumina as supports for Ni_2P. *Fuel* **264**, 116764. https://doi.org/10.1016/j.fuel.2019.116764.

Merlo, M. A., Jaimes, D. A., Escrig, J., Pérez, O. L. & Bajales, N. 2021 Carbon-coated alumina nanochannels-based composite: A conductivity analysis by means of electrochemical impedance spectroscopy. *Materials Letters* **295**, 129795. https://doi.org/10.1016/j.matlet.2021.129795.

Miranda, A. C., Lepretti, M., Rizzo, L., Caputo, I., Vaiano, V., Sacco, O., Lopes, W. S. & Sannino, D. 2016 Surface water disinfection by chlorination and advanced oxidation processes: Inactivation of an antibiotic resistant E. coli strain and cytotoxicity evaluation. *Science of the Total Environment* **554**, 1–6. https://doi.org/10.1016/j.scitotenv.2016.02.189.

Monson, P. A. 2012 Understanding adsorption/desorption hysteresis for fluids in mesoporous materials using simple molecular models and classical density functional theory. *Microporous and Mesoporous Materials* **160**, 47–66. https://doi.org/10.1016/j.micromeso.2012.04.043.

Morshed, M. N., Bouazizi, N., Behary, N., Guan, J. & Nierstrasz, V. 2019 Stabilization of zero valent iron (Fe^0) on plasma/dendrimer functionalized polyester fabrics for Fenton-like removal of hazardous water pollutants. *Chemical Engineering Journal* **374**, 658–673. https://doi.org/10.1016/j.cej.2019.05.162.

Muñoza, I., Rodríguezb, A., Rosalb, R. & Fernández-Albaa, A. R. 2008 Life cycle assessment of urban wastewater reuse with ozonation as tertiary treatment. https://doi.org/10.1016/j.scitotenv.2008.09.029.

Nagarajan, D. & Venkatanarasimhan, S. 2019 Copper (II) oxide nanoparticles coated cellulose sponge – an effective heterogeneous catalyst for the reduction of toxic organic dyes. *Environmental Science and Pollution Research* **26**, 22958–22970. https://doi.org/10.1007/s11356-019-05419-0.

Nair, M. G., Nirmala, M., Rekha, K. & Anukaliani, A. 2011 Structural, optical, photo catalytic and antibacterial activity of ZnO and Co doped ZnO nanoparticles. *Materials Letters* **65**(12), 1797–1800. https://doi.org/10.1016/j.matlet.2011.03.079.

Navío, J. A., Colón, G., Macías, M., Real, C. & Litter, M. I. 1999 Iron-doped titania semiconductor powders prepared by a sol–gel method. Part I: Synthesis and characterization. *Applied Catalysis A: General* **177**(1), 111–120. https://doi.org/10.1016/S0926-860X(98)00255-5.

Nenavathu, B. P., Kandula, S. & Verma, S. 2018 Visible-light-driven photocatalytic degradation of safranin-T dye using functionalized graphene oxide nanosheet (FGS)/ZnO nanocomposites. *RSC Advances* **8**(35), 19659–19667. https://doi.org/10.1039/c8ra02237b.

Nishikiori, H., Sato, T., Kubota, S., Tanaka, N., Shimizu, Y. & Fujii, T. 2012 Preparation of Cu-doped TiO_2 via refluxing of alkoxide solution and its photocatalytic properties. *Research on Chemical Intermediates* **38**, 595–613. https://doi.org/10.1007/s11164-011-0374-z.

Ong, C. B., Ng, L. Y. & Mohammad, A. W. 2018 A review of ZnO nanoparticles as solar photocatalysts: Synthesis, mechanisms and applications. *Renewable and Sustainable Energy Reviews* **81**, 536–551. https://doi.org/10.1016/j.rser.2017.08.020.

Paek, C., McCormick, A. V. & Carr, P. W. 2010 Preparation and evaluation of carbon coated alumina as a high surface area packing material for high performance liquid chromatography. *Journal of Chromatography A* **1217**, 6475–6483.

Pascariu, P., Tudose, I. V., Suchea, M., Koudoumas, E., Fifere, N. & Airinei, A. 2018 Preparation and characterization of Ni, Co doped ZnO nanoparticles for photocatalytic applications. *Applied Surface Science* **448**, 481–488. https://doi.org/10.1016/j.apsusc.2018.04.124.

Pierce, J. 1994 Colour in textile effluents-the origins of the problem. *Journal of the Society of Dyers and Colourists* **110**(4), 131–133. https://doi.org/10.1111/j.1478-4408.1994.tb01624.x.

Poornaprakash, B., Chalapathi, U., Subramanyam, K., Vattikuti, S. P. & Park, S. H. 2020 Wurtzite phase Co-doped ZnO nanorods: morphological, structural, optical, magnetic, and enhanced photocatalytic characteristics. *Ceramics International* **46**(3), 2931–2939. https://doi.org/10.1016/j.ceramint.2019.09.289.

Praveen, R., Chandreshia, C. B. & Ramaraj, R. 2018 Silicate sol–gel matrix stabilized ZnO–Ag nanocomposites materials and their environmental remediation applications. *Journal of Environmental Chemical Engineering* **6**(3), 3702–3708. https://doi.org/10.1016/j.jece.2017.01.048.

Ravidhas, C., Josephine, A. J., Sudhagar, P., Devadoss, A., Terashima, C., Nakata, K., Fujishima, A., Raj, A. M. E. & Sanjeeviraja, C. 2015 Facile synthesis of nanostructured monoclinic bismuth vanadate by a co-precipitation method: Structural, optical and photocatalytic properties. *Materials Science in Semiconductor Processing* **30**, 343–351. https://doi.org/10.1016/j.mssp.2014.10.026.

Reddy, I. N., Reddy, C. V., Shim, J., Akkinepally, B., Cho, M., Yoo, K. & Kim, D. 2020 Excellent visible-light driven photocatalyst of (Al, Ni) co-doped ZnO structures for organic dye degradation. *Catalysis Today* **340**, 277–285. https://doi.org/10.1016/j.cattod.2018.07.030.

Rochkind, M., Pasternak, S. & Paz, Y. 2014 Using dyes for evaluating photocatalytic properties: A critical review. *Molecules* **20**(1), 88–110. https://doi.org/10.3390/molecules20010088.

Salem, J. K., Hammad, T. M. & Harrison, R. R. 2013 Synthesis, structural and optical properties of Ni-doped ZnO micro-spheres. *Journal of Materials Science: Materials in Electronics* **24**, 1670–1676. https://doi.org/10.1007/s10854-012-0994-0.

Sapkota, K. P., Lee, I., Hanif, M. A., Islam, M. A. & Hahn, J. R. 2019 Solar-light-driven efficient ZnO–single-walled carbon nanotube photocatalyst for the degradation of a persistent water pollutant organic dye. *Catalysts* **9**(6), 498. https://doi.org/10.3390/catal9060498.

Sarmah, K., Roy, U. K., Maji, T. K. & Pratihar, S. 2018 Role of metal exchange toward the morphology and photocatalytic activity of Cu/Ag/Au-Doped ZnO: A study with a zinc–Sodium acetate complex as the precursor. *ACS Applied Nano Materials* **1**(5), 2049–2056. https://doi.org/10.1021/acsanm.8b00436.

Senasu, T., Chankhanittha, T., Hemavibool, K. & Nanan, S. 2021 Visible-light-responsive photocatalyst based on ZnO/CdS nanocomposite for photodegradation of reactive red azo dye and ofloxacin antibiotic. *Materials Science in Semiconductor Processing* **123**, 105558. https://doi.org/10.1016/j.mssp.2020.105558.

Senthilkumar, S., Basha, C. A., Perumalsamy, M. & Prabhu, H. J. 2012 Electrochemical oxidation and aerobic biodegradation with isolated bacterial strains for dye wastewater: Combined and integrated approach. *Electrochimica Acta* **77**, 171–178. https://doi.org/10.1016/j.electacta.2012.05.084.

Sharanda, L. F., Plyuto, Y. V., Babich, I. V., Plyuto, I. V., Shpak, A. P., Stoch, J. & Moulijn, J. A. 2006 Synthesis and characterisation of hybrid carbon-alumina support. *Applied Surface Science* **252**(24), 8549–8556. https://doi.org/10.1016/j.apsusc.2005.11.078.

Shashikala, V., Kumar, V. S., Padmasri, A. H., Raju, B. D., Mohan, S. V., Sarma, P. N. & Rao, K. R. 2007 Advantages of nano-silver-carbon covered alumina catalyst prepared by electro-chemical method for drinking water purification. *Journal of Molecular Catalysis A: Chemical* **268**(1–2), 95–100. https://doi.org/10.1016/j.molcata.2006.10.019.

Shinde, K. P., Pawar, R. C., Sinha, B. B., Kim, H. S., Oh, S. S. & Chung, K. C. 2014 Optical and magnetic properties of Ni doped ZnO planetary ball milled nanopowder synthesized by co-precipitation. *Ceramics International* **40**(10), 16799–16804. https://doi.org/10.1016/j.ceramint.2014.07.148.

Sing, K. S. W., Everett, D. H., Haul, R. A. W., Moscou, L., Pierotti, R. A., Rouquerol, J. & Siemieniewska, T. 1985 Reporting physisorption data forgas/solid systems with special reference to the determination of surface area and porosity. *Pure Appl Chem* **57**(4), 603–609. https://doi.org/10.1351/pac198557040603.

Singh, S., Sharma, R. & Mehta, B. R. 2017 Enhanced surface area, high Zn interstitial defects and band gap reduction in N-doped ZnO nanosheets coupled with BiVO4 leads to improved photocatalytic performance. *Applied Surface Science* **411**, 321–330. https://doi.org/10.1016/j.apsusc.2017.03.189.

Skinner, A. W., DiBernardo, A. M., Masud, A. M., Aich, N. & Pinto, A. H. 2020 Factorial design of experiments for optimization of photocatalytic degradation of tartrazine by zinc oxide (ZnO) nanorods with different aspect ratios. *Journal of Environmental Chemical Engineering* **8**(5), 104235. https://doi.org/10.1016/j.jece.2020.104235.

Solodovnichenko, V. S., Simunin, M. M., Lebedev, D. V., Voronin, A. S., Emelianov, A. V., Mikhlin, Y. L., Parfenov, V. A. & Ryzhkov, I. I. 2019 Coupled thermal analysis of carbon layers deposited on alumina nanofibres. *Thermochimica Acta* **675**, 164–171. https://doi.org/10.1016/j.tca.2019.02.012.

Souza Macedo, L., Teixeira da Silva, V. & Bitter, J. H. 2019 Activated carbon, carbon nanofibers and carbon-covered alumina as support for W_2C in stearic acid hydrodeoxygenation. *ChemEngineering* **3**(1), 24. https://doi.org/10.3390/chemengineering3010024.

Srinivasan, N., Anbuchezhiyan, M., Harish, S. & Ponnusamy, S. 2019 Hydrothermal synthesis of C doped ZnO nanoparticles coupled with $BiVO_4$ and their photocatalytic performance under the visible light irradiation. *Applied Surface Science* **494**, 771–782. https://doi.org/10.1016/j.apsusc.2019.07.093.

Sun, X., Cheng, C., Shen, J., Liu, Y., Wang, T., Ma, Q. & Fan, R. 2020 Fine-tuning of negative permittivity behavior in amorphous carbon/alumina metacomposites. *Ceramics International* **46**(7), 8942–8948. https://doi.org/10.1016/j.ceramint.2019.12.141.

Taka, A. L., Pillay, K. & Mbianda, X. Y. 2017 Nanosponge cyclodextrin polyurethanes and their modification with nanomaterials for the removal of pollutants from waste water: A review. *Carbohydrate Polymers* **159**, 94–107. https://doi.org/10.1016/j.carbpol.2016.12.027.

Tang, X., Zheng, H., Teng, H., Sun, Y., Guo, J., Xie, W., Yang, Q. & Chen, W. 2016 Chemical coagulation process for the removal of heavy metals from water: A review. *Desalination and Water Treatment* **57**(4), 1733–1748. https://doi.org/10.1080/19443994.2014.977959.

Thommes, M., Kaneko, K., Neimark, A. V., Olivier, J. P., Rodriguez-Reinoso, F., Rouquerol, J. & Sing, K. S. 2015 Physisorption of gases, with special reference to the evaluation of surface area and pore size distribution (IUPAC technical report). *Pure and Applied Chemistry* **87**(9–10), 1051–1069. https://doi.org/10.1515/pac-2014-1117.

Tonda, S., Kumar, S., Kandula, S. & Shanker, V. 2014 Fe-doped and-mediated graphitic carbon nitride nanosheets for enhanced photocatalytic performance under natural sunlight. *Journal of Materials Chemistry A* **2**(19), 6772–6780. https://doi.org/10.1039/C3TA15358D.

Tran Thi, V. H., Pham, T. N., Pham, T. T. & Le, M. C. 2019 Synergistic adsorption and photocatalytic activity under visible irradiation using Ag-ZnO/GO nanoparticles derived at low temperature. *Journal of Chemistry* **2019**. https://doi.org/10.1155/2019/2979517.

Udom, I., Ram, M. K., Stefanakos, E. K., Hepp, A. F. & Goswami, D. Y. 2013 One dimensional-ZnO nanostructures: Synthesis, properties and environmental applications. *Materials Science in Semiconductor Processing* **16**(6), 2070–2083. https://doi.org/10.1016/j.mssp.2013.06.017.

Wu, Z., Chen, X., Liu, X., Yang, X. & Yang, Y. 2019 A ternary magnetic recyclable ZnO/Fe_3O_4/Gc_3N_4 composite photocatalyst for efficient photodegradation of monoazo dye. *Nanoscale Research Letters* **14**, 1–14. https://doi.org/10.1186/s11671-019-2974-2.

Xu, B., Yang, Y., Xu, Y., Han, B., Wang, Y., Liu, X. & Yan, Z. 2017 Synthesis and characterization of mesoporous Si-modified alumina with high thermal stability. *Microporous and Mesoporous Materials* **238**, 84–89. https://doi.org/10.1016/j.micromeso.2016.02.031.

Yang, Y., Ma, J. & Wu, F. 2006 Production of hydrogen by steam reforming of ethanol over a Ni/ZnO catalyst. *International Journal of Hydrogen Energy* **31**(7), 877–882. https://doi.org/10.1016/j.ijhydene.2005.06.029.

Yang, X., Tian, J., Guo, Y., Teng, M., Liu, H., Li, T., Lv, P. & Wang, X. 2021 Zno nano-rod arrays synthesized with exposed {0001} facets and the investigation of photocatalytic activity. *Crystals* **11**(5), 522. https://doi.org/10.3390/cryst11050522.

Yarahmadi, A. & Sharifnia, S. 2014 Dye photosensitization of ZnO with metallophthalocyanines (Co, Ni and Cu) in photocatalytic conversion of greenhouse gases. *Dyes and Pigments* **107**, 140–145. https://doi.org/10.1016/j.dyepig.2014.03.035.

Yu, F., Cao, L., Huang, J. & Wu, J. 2013 Effects of pH on the microstructures and optical property of FeWO4 nanocrystallites prepared via hydrothermal method. *Ceramics International* **39**(4), 4133–4138. https://doi.org/10.1016/j.ceramint.2012.10.269.

Zheng, M., Shu, Y., Sun, J. & Zhang, T. 2008 Carbon-covered alumina: A superior support of noble metal-like catalysts for hydrazine decomposition. *Catalysis Letters* **121**, 90–96. https://doi.org/10.1007/s10562-007-9300-9.

Zollinger, H. 2003 *Color Chemistry: Syntheses, Properties, and Applications of Organic Dyes and Pigments*, 3rd edn. Wiley-VCH, Weinheim, Germany.

First received 17 April 2023; accepted in revised form 21 July 2023. Available online 2 August 2023